Syracuse University
SURFACE at Syracuse University

Theses - ALL

Summer 7-16-2021

Computational Investigation of Biological Membranes

Allyson Karmazyn
Syracuse University

Follow this and additional works at: https://surface.syr.edu/thesis

 Part of the Biomedical Engineering and Bioengineering Commons, and the Chemical Engineering Commons

Recommended Citation

Karmazyn, Allyson, "Computational Investigation of Biological Membranes" (2021). *Theses - ALL*. 568.
https://surface.syr.edu/thesis/568

This Thesis is brought to you for free and open access by SURFACE at Syracuse University. It has been accepted for inclusion in Theses - ALL by an authorized administrator of SURFACE at Syracuse University. For more information, please contact surface@syr.edu.

Abstract

Lipids are the building blocks of biological membranes, and the types of lipids that compose these cellular envelopes influence the physicochemical properties of the chemicals that can enter or exit the cell across the membrane. This work focuses on the lipid membrane compositions of eukaryotic (red blood cells) and prokaryotic (*Pseudomonas aeruginosa*) membranes. By analyzing the lipid-lipid and lipid-protein interactions results of the computational simulations, insights into lipid aggregation, bilayer leaflet behavior, membrane asymmetry, and small molecule transport through protein channels were obtained. The differences between prokaryotic and eukaryotic cell membranes are qualitative known; however, this work provides these concepts through quantitative evidence using multiscale molecular dynamics simulations. The results show that membrane leaflet asymmetry affects the membrane properties and protein-lipid interactions. The CLASP algorithm was employed to efficiently simulate the transport of small molecules through a bacterial membrane porin and analyze the resulting contacts of that molecule with the pore-lining residues.

Computational investigation of biological membranes

by

Allyson Karmazyn

Bioengineering

B.S., Syracuse University, 2020

Thesis
Submitted in Partial Fulfillment of the Requirements of
the Master of Science in Bioengineering

Syracuse University
July 2021

Copyright © Allyson Karmazyn 2021

All Rights Reserved

Acknowledgements

I would like the thank my principal investigator and advisor, Shikha Nangia, Ph.D., for providing me with the environment and opportunity to conduct my research. I am beyond grateful for your guidance and inspiration that has allowed me to grow into the researcher I am today. I will always carry your lessons and enthusiasm for research with me into my future endeavors. Thank you.

I would also like the acknowledge Nandhini Rajagopal, Ph.D. and Yinghui Dai, a doctoral candidate, for taking me under their wings in the lab. Nandhini taught me the ropes of the computational research when I first began my research and provided me with an amazing foundation of the experimental protocols and research. I worked side-by-side with Yinghui, and we developed not only an efficient and enjoyable research collaboration, but a friendship. I thank you Yinghui for your constant availability and openness that fostered this academic and personal relationship and I wish you all the success in your future work.

I would like to thank the entire Nangia Research Group where I began as an eager learner and evolved into a mentor over the years. This group allowed me to expand my curiosity for research and increase my confidence in computational simulations by teaching new lab members. This group will always have a special place in my heart.

Lastly, I would like to thank the College of Engineering and Computer Science at Syracuse University, and more specifically the Department of Biomedical and Chemical Engineering, for the academic knowledge that fostered my love for research. I have developed lasting relationships with fellow students and faculty, and I will cherish the memories I have made in this community.

Table of Contents

CHAPTER I – Fingerprinting plasma membrane lipidome of human red blood cells using computational modeling techniques

Background

***Lipidomics*[1].** The rapid development of genomics technology, specifically mass spectroscopy, has provided immense insight into cell processes and the metabolites that drive these behaviors. Metabolomics is studied for healthy and diseased cells with lipidomics reserving its own field of exploration. A lipidome is a comprehensive profile of lipid types that is specific to a cell type and the characteristic of these lipids to inherently self-assemble into bilayer membranes provides insight into the intra- and intercellular pathways of a cell. The study of lipidomics provides details on lipid type concentrations in a cellular membrane and their respective locations in the bilayer as well as the leaflet. The interactions between lipid types are important to note because this can determine properties of lipid-lipid and lipid-protein interactions which can be useful for delivery and transport research for diseased cells. Cell membranes composition can be influenced by diet[2], among other environmental factors, resulting in diseased cells and disrupting the homeostasis the cell works very hard to maintain. Such diseases linked to changes in lipid composition include cancers, HIV, diabetes, atherosclerosis, cardiovascular disease, and Alzheimer's disease. To study these diseases and discover methods to combat or reverse their effects, lipidomics research can identify the change in lipid concentration and position over time providing more information concerning transport pathways and their respective proteins. Lipidomics can map the composition of cell type plasma membranes as well as individual membrane-bound organelles in those respective cell types.

***Computational Modeling*[3].** Computational modeling systems (CMS) are tools that allow scientists and researchers to efficiently study complex systems through mathematical- and physics-based algorithms. This iterative modeling technique allows high-throughput testing of systems in a comprehensive environment that can be tailored to the researcher's needs. The computational platform provides a wide range of modeling tools depending on the subject matter being studied, which can be made even more efficient through different representation methods and manipulation of code scripts. Computational systems allow scientists to provide educated inferences to experimental researchers based on generated representational structures (R-structures) and quantitative data approximations. The computational modeling methods provide researchers with the ability to manipulate experimental variables while modifying the protocols to develop even more logical workflows. A system can be represented by innumerable models that are all equivalent in nature, however it is the researcher's decision of which model to use, the manipulations applied to the model, and the efficiency of generating such a model. The extraordinary capabilities of computational modeling scientific applications provide researchers with more freedom to tune experiments in a faster and individualized way.

***Simulation Methods Hierarchy*[4].** The hierarchical organization of simulation methods was developed on the multiscale modeling which is the simultaneous implementation of multiple models at different scales for analyzing a system. These different

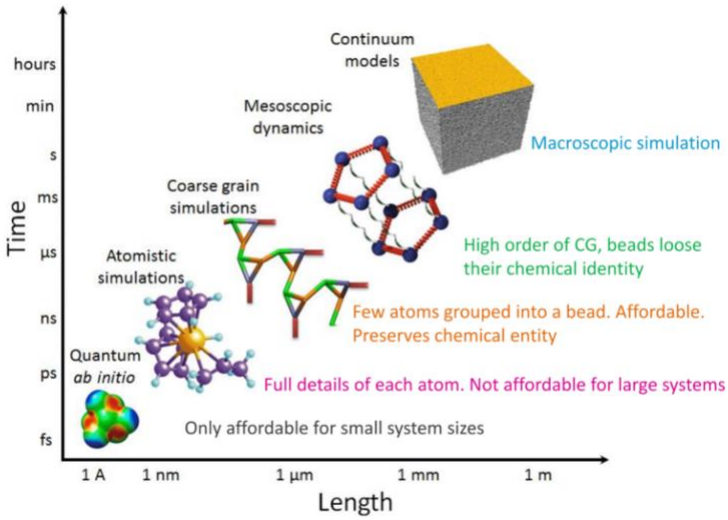

Figure 1. Simulation methods hierarchy schematic plotted based on time scale and structure length.

scales utilized different levels of resolution; with macroscale models being too broad and not accurate enough to microscale models being not efficient enough and too specific. Researchers employing multiscale modeling can move between hierarchical levels to ensure the simulation and resulting information fit their needs. Multiscale modeling unifies three components: (1) analysis allowing researchers to understand the dynamic relationship between the different resolutions, (2) models providing visual representations of the coupling of different scales, and (3) algorithms implementing multiscale concepts to produce results. The two resolutions used most often in biomolecular simulations are atomistic and coarse grain simulations that are categorized under molecular dynamics. Atomistic simulations are conducted on the microsecond timescale and in the nanoscale. This method maintains the full detail of each atom in the system; however, it is not very affordable computationally. Coarse grain simulations are conducted on the millisecond timescale and in the nanoscale and follow a mapping pattern by grouping approximately 4 atoms to form a bead. This method is computationally affordable while preserving the chemical entity of the system. These two methods are easily comparable by utilizing reverse mapping algorithms.

Molecular Dynamics[5]. Molecular Dynamics (MD) is a computational simulation method of the physical movements of atoms and molecules of a system that can be used for studying the physical and chemical properties of solids, liquids, amorphous materials, and biological molecules. Although quantum mechanics is the accepted theory for studying molecular interactions, MD is used to simulate these interactions using Newton's law of motion and set environmental parameters to produce accurate results. The trajectories of the atoms of an MD system are collected via an iterative process of positions over a specified time period at each time step. A box-shaped environment is constructed for the system and each atom's position is

recorded as an x, y, and z-coordinate and corresponds to the time step in which it is in that coordinate. As the particles in the system undergo changes in position, they experience interactive forces from other particles and forces can be calculated for an individual atom or molecule and the forces acting on it to produce a net force. The change in position of the particle is ultimately calculated by an algorithm based on the known mass of the atom or molecule and its change in velocity at a given time. A limitation in MD is that the boundaries of the box housing the system can interact with the particles causing discrepancies in the data. However, the addition of boundary conditions can be applied to allow for an infinite replication of the box to allow particles to bass through the box walls, which can be visualized by periodically translating the box in a visual molecular dynamics (VMD) software. Furthermore, position restraints can be applied to the system or individual particles as needed based on the simulation.

Introduction

Lipids[7]**.** Lipids are defined as biological molecules that are present in all cells and aggregate in order to construct membrane matrices. The lipid category of molecules is comprised on many subfamilies with their own properties; however, all lipids are similar in that they are extremely hydrophobic and moderately soluble in water. The general functions of lipids are (1) to form bilayer membranes of cells and organelles, (2) to store energy if lipid contains hydrocarbon chains, and (3) to participate in intra- and intercellular signaling events. This work focuses on glycerophospholipids which are

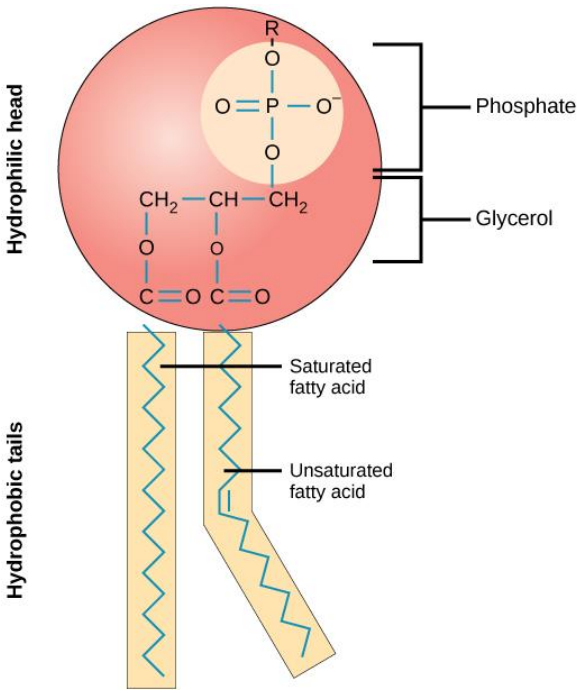

Figure 2. Representative phospholipid structure[6].

composed of a polar head and a nonpolar fatty acid tail. The polar head consists of a phosphate group, a glycerol group, and an alcohol group. Lipid families are differentiated by the alcohol present in the headgroup. The fatty acid tails are bonded to the headgroup via an ester bond. Glycerophospholipids can be saturated; does not contain any double bonds in fatty acid carbon tails, unsaturated; contains one double bond in fatty acid tails, or polyunsaturated; contains two or more double bonds in fatty acid tails.

Bilayer Membranes. Lipid bilayer membranes contain two layers of aggregate lipids (composition based on cell type) and form due their amphiphilic properties. This bilayer arrangement is driven by the hydrophobic repulsion of the fatty acid tails from water and the hydrophilic properties of the headgroups. The bilayer consists of an exoplasmic leaflet that faces the outside of the cell and a cytoplasmic leaflet that shares a barrier with the cytoplasm of the cell. The membrane functions as the gate between the biological environment and the inside of the cell and facilitates transport of molecules via embedded protein channels. The characteristics of the membrane, types of proteins embedded in the membrane, and lipid composition are determined by the structure and function of the specific cell type.

Red Blood Cells[8]. Red blood cells (RBCs) are the cellular component of blood that are tasked with carrying oxygen from the lungs to the tissues and conversely carry carbon dioxide to the lungs for excretion. A mature RBC is round and biconcave to allow for transport through very small blood vessels. These cells contain a membrane bilayer with proteins and hemoglobin while lacking a nucleus. RBCs are developed in bone marrow beginning as a type of multipotent mesenchymal stem cell termed a hemocytoblast and differentiates into an erythroblast. The erythroblast then fills with hemoglobin and the cell's nucleus and cytoplasm are eliminated. In

the last stage of differentiation, the cell is termed a reticulocyte which becomes a fully mature RBC. On average, an adult human has approximately 5.2 million red blood cells per cubic millimeter of blood. In some cases, red blood cells can present an abnormal shape as in pernicious anemia (oval), sickle cell anemia (crescent), and acanthocytosis (spiked). There is a critical need for research into the physiochemical properties and biological function of asymmetrical RBC membranes.

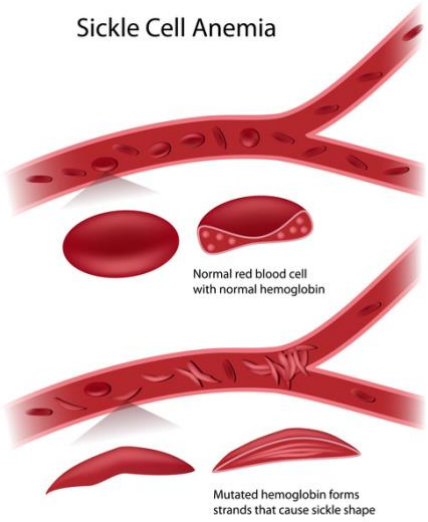

Figure 3. Normal red blood cell structure versus red blood cells of an individual with sickle cell anemia[9].

Experimental Overview. Advances in membrane lipidomics have revealed a rich chemical diversity and leaflet asymmetry in eukaryotic cells[1,10-16] which contrast the rudimentary fluid-mosaic model of cell membranes that depicted the membrane as a simple mixture of lipids that accommodated membrane proteins[17-18]. In addition to functioning as a cell's first line of defense, the plasma membrane (PM) is a highly functional interface for many signals transduction events to occur mediated via peripheral and membrane-embedded proteins[19-23]. The leaflet asymmetry of the plasma membrane is evident in various eukaryotic cells—red blood cells (RBCs), platelets, and neuronal cells.

The lipid diversity manifests in two ways: (i) chemical structure of the lipids—charge, and type of the headgroups, length of the acyl chains, and the number and location of double bonds in the acyl chain backbone; and (ii) compositional diversity—the proportion of lipids in membrane leaflets[24]. These variations confer each leaflet its distinct biophysical property to

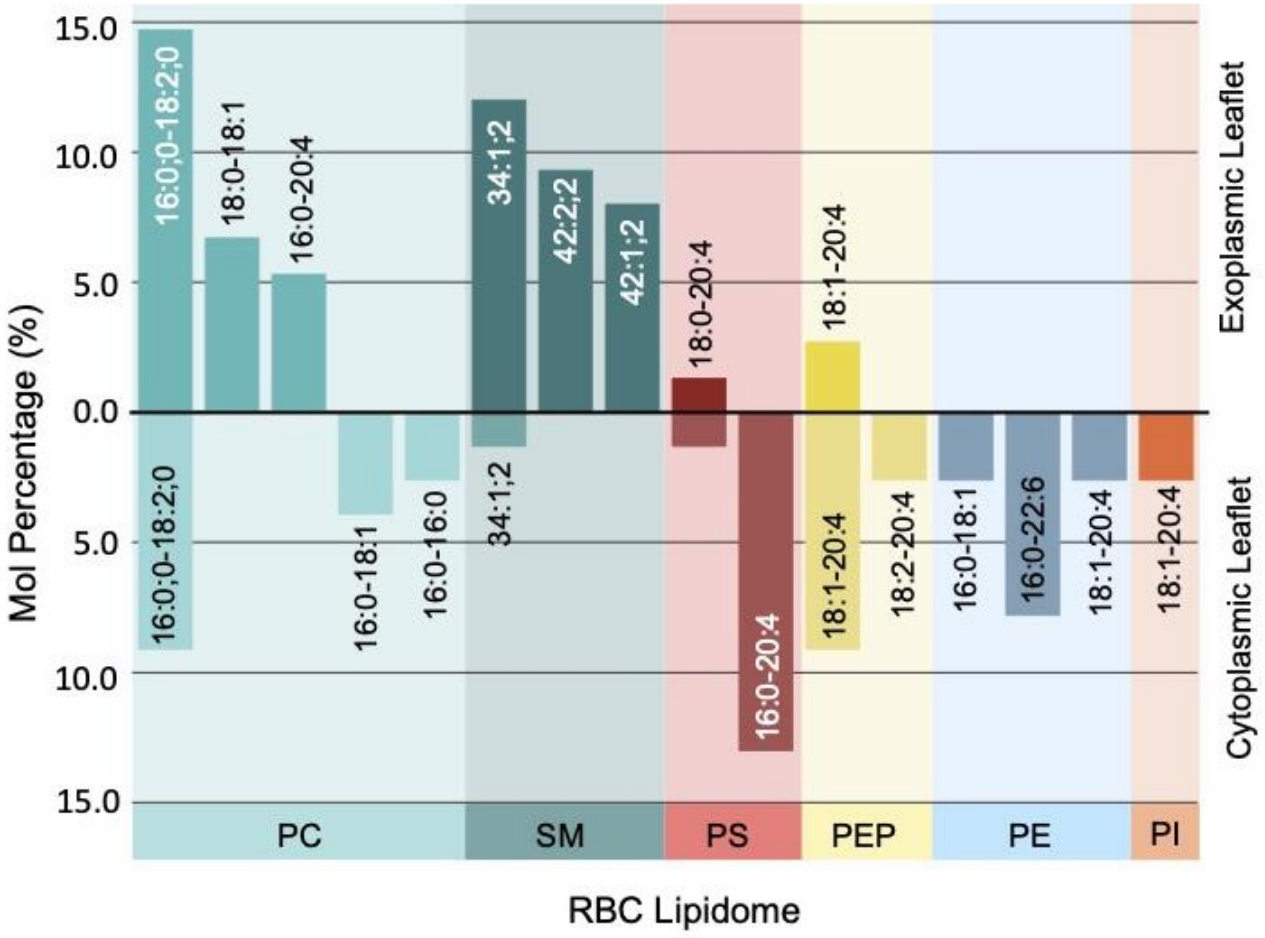

Figure 4. RBC plasma membrane composition distribution in exoplasmic leaflet and cytoplasmic leaflet. Lipids separated by category, phosphatidylcholine (PC, cyan), sphingomyelin (SM, dark cyan), phosphatidylserine (PS, red), phosphatidylethanolamine plasmalogen (PEP, yellow), phosphatidylethanolamine (PE, blue), and phosphatidylinositol (PI, orange). Lipid species annotated as (total number of carbon atoms in the acyl chain):(total number of double bonds in acyl chains);(total number of hydroxyl groups in the long acyl chain).

interface with the cell's external and internal environment[12-13]. In a recent study, human RBC plasma membrane's leaflet asymmetry and distinct compositions of the exoplasmic and cytosolic leaflets were reported[25]. The results showed that compared to the cytosolic leaflet (CL), the exoplasmic leaflet (EL) is more densely packed and rich in lipids with a higher percentage of saturated lipids. Specifically, the EL is composed of phosphatidylcholine (PC), sphingomyelins (SM) with one or more unsaturations per acyl chain, and a small percentage of phosphatidylserine (PS) and phosphatidylethanolamine plasmalogen (PEP). On the contrary, the CL has higher lipid headgroup diversity, including phosphatidylethanolamine (PE),

phosphatidylinositol (PI), PS, PC, SM, and PEP. Although cholesterol was reported in both leaflets, the experimental analysis did not directly provide the cholesterol distribution[25]. The detailed lipid distribution within the major lipid families is reproduced in Figure 4.

Despite the evidence of plasma membrane leaflet asymmetry, RBC membrane leaflet's physicochemical properties and biological function needs more research to formulate a comprehensive description. The unique lipid composition of each leaflet impacts the membrane's biophysical properties: cholesterol distribution (flip-flop rate, domain formation, and oligomerization); membrane thickness (lipid interdigitation at membrane mid-plane); surface charge (lipid headgroup distribution); membrane protein distribution (protein hydrophobic thickness and shape); and membrane protein's post-translational modifications (CL versus EL).

Several computational studies have focused on the structure and dynamics of model cell membranes with variable lipid complexities and compositions[26-42]. Ingólfsson et al. modeled an idealized plasma membrane consisting of 63 different lipid species that were asymmetrically distributed across the two leaflets[33]. Other computational studies have investigated asymmetric cholesterol distribution in the lipid bilayers[43-49]. A recent study explored the relationship between cholesterol distribution leaflet lipid order; the more ordered the leaflet, the higher its cholesterol concentration—the type of lipids in the leaflet influence the cholesterol distribution and the flip-flop rate between the leaflets[49]. These model membranes have been critical in building a foundation for deciphering molecular level lipid-lipid interactions.

However, the human RBC plasma membrane lipidome is more complex than an idealized model membrane previously investigated by computational techniques. In this work, the structural and compositional diversities in RBC membrane leaflets using molecular dynamics at the coarse-grained (CG) resolution are investigated. Martini force field parameters[54-56] are used

as they have been widely used to investigate biomembranes[36,49,57-60] and proteins[49,55,56-57,61-67]. The parameter sets for a subset of PI, SM, PE, and PEP lipids unavailable in the Martini force field were developed in this work. The results show the different lipid type's behaviors in terms of the lipid-lipid mixing parameters, lipid order parameters in the membrane leaflets, cholesterol distribution, leaflet densities, and membrane thickness.

Methods

Martini Force Field Parameters. The Martini CG parameters are based on a many-to-one mapping scheme, in which four neighboring non-hydrogen atoms are mapped into one CG bead[54-56,68-69]. Martini allows some flexibility to adopt a three-to-one or five-to-one mapping scheme, if required, to preserve properties in the chemical structures. The RBC membrane contains several lipids (Table 1) with the following lipid families: PC (PIPC, POPC, PAPC, and DPPC); SM (DPSM, PNSM, and PLSM); PEP (PEP1 and PEP2); PE (POPE, PUPE, and PEPE); PS (PAPS and PAPS2); and PI (PIP2). The Martini force field parameters are available for most of the RBC membrane lipids (PIPC, POPC, PAPC, DPPC, PAPS, PAPS2, POPE, PUPE, PAPS, and CHOL). For the remaining lipids, the parameters were constructed using the Martini headgroup and acyl chain bead types. The current Martini parameter database does not include an SM lipid with only one unsaturation, which is inherently present in the sphingosine backbone (18:1) of all sphingomyelin lipids. Therefore, we built the parameters for PLSM (42:1;2), which translates into PLSM (18:1-24:0), according to the Martini nomenclature. Additionally, unlike the available PE lipids, the PEP lipids possess a vinyl-ether linkage at the sn-1 position instead of an ester linkage and an ester linkage at the sn-2 position,65 for which Martini parameters had to be developed. The parameter sets for the newly developed lipids—PLSM, PEP1, PEP2, PEPE, and PIP2 (Table A1-A5) are available for download from the Nangia research website.

Table 1. Lipid abbreviations and corresponding head groups and tails.

Lipid Abbreviation	Lipid Head Group	Lipid Tails
PIPC	Phosphatidylcholine (PC)	16:0;0-18:2;0
POPC	Phosphatidylcholine (PC)	18:0-18:1
PAPC	Phosphatidylcholine (PC)	16:0-20:4
POPC	Phosphatidylcholine (PC)	16:0-18:1
DPPC	Phosphatidylcholine (PC)	16:0-16:0
DPSM	Sphingomyelin (SM)	34:1;2
PNSM	Sphingomyelin (SM)	42:2;2
PLSM	Sphingomyelin (SM)	42:1;2
PAPS	Phosphatidylserine (PS)	18:0-20:4
PAPS2	Phosphatidylserine (PS)	16:0-20:4
PEP1	Phosphatidylethanolamine plasmalogen (PEP)	18:1-22:4
PEP2	Phosphatidylethanolamine plasmalogen (PEP)	18:2-20:4
POPE	Phosphatidylethanolamine (PE)	16:0-18:1
PUPE	Phosphatidylethanolamine (PE)	16:0-22:6
PEPE	Phosphatidylethanolamine (PE)	18:1-20:4
PIP2	Phosphatidylinositol (PI)	18:0-22:4

Lipid Membrane. A 30×30 nm^2 patch membrane mimicking the human RBC plasma membrane composition was constructed in the CG resolution using a locally modified insane.py script[70]. The newly developed lipids are included in this modified insane.py script. The membrane EL and CL consisted of the specific lipid compositions presented previously. The membrane was placed in a 30×30×15 nm^3 simulation box and solvated with standard Martini water (9:1 of W:WF) and 150 mM NaCl.

CG MD Simulations. The GROMACS 5.1.2 package[71] was used for all MD simulations. The system was energy minimized until the maximum force on any bead was below the tolerance parameter of 10 $kJmol^{-1}nm^{-1}$. The minimization was followed by equilibration in isothermal-isochoric (NVT) conditions for 25 ns, followed by a two-step isothermal-isobaric NPT (NPT1 and NPT2) equilibration for 30 and 45 ns, respectively. Position restraints were used at lipid PO4 headgroup beads in NVT, NPT1, and NPT2 with a force constant set at 100, 10, and 5 $kJmol^{-1}$ nm^{-1}, respectively. A 20 fs time step was used for the equilibration and production runs. The

temperature was maintained at 300 K for all systems using the v-rescale[72] thermostat with $\tau t = 1$ ps. A semi-isotropic pressure coupling of 1 bar was maintained using Parrinello-Rahman barostat[73] with $\tau p = 8$ ps. Both the nonbonded van der Waals and the electrostatic interaction cut-offs were set to 1.1 nm. The potential-shift-Verlet algorithm was applied to shift the van der Waals interactions beyond the cut-off. The Coulombic interactions were calculated using the reaction-field algorithm. Periodic boundary conditions were applied in all three dimensions (x, y, and z-direction). All position restraints were removed in the production runs. Flat-bottomed position restraints were applied to the phosphate beads of the lipid at 2.5 nm above and below the membrane with force constant of 1000 $kJmol^{-1}nm^{-2}$. The simulations were performed in triplicates, each for five microseconds, determined by the convergence of mixing parameters plots. Thermal annealing simulations were performed from 280 K to 320 K with 5 K interval; each temperature step was equilibrated for 500 ns.

Mixing Parameter. Mixing parameter analyses are performed using multiple, in-house developed python scripts with molecular visualization generated using VMD and PyMOL software. The mixing parameter of membrane lipids is calculated as $p_{ij} = \frac{C_{ij}}{\sum C_{ik}}$ where p_{ij} is the mixing parameter between lipid i and lipid j, C_{ij} is the number of contacts made by lipid i with lipid j, and $\sum C_{ik}$ is the total contacts made by lipid i with all surrounding lipids, including itself. A contact is defined to have formed between two lipid molecules if the distance between a lipid species and the reference lipid is within a 1.1 nm cut-off.

Order Parameter. The order parameter of lipid acyl chain is calculated from ^2H NMR as $S_{CD} = \langle\frac{3\cos^2\theta-1}{2}\rangle$, where S_{CD} is the order parameter between the carbon-hydrogen (C−D) bond, θ is the angle between the C−D bond vector and a reference axis, which is the membrane normal x ,y, z = 0,0,1. The angular brackets determine that order parameters are weighted over time. Two types

of order parameters are evaluated, in viewpoint of carbon beads, order parameter was calculated between every two adjacent carbon beads and averaged over lipids of the exoplasmic leaflet (EL) and the cytoplasmic leaflet (CL), respectively. For the other purpose of analysis, each entire lipid acyl chain is calculated with one order parameter generated, averaging over lipids of the same type in EL and CL, respectively.

Cholesterol Flip-Flop. The cholesterol flip-flop rate is calculated as an average frequency of the intermembrane flipping of cholesterol. Cholesterol flipping is identified when the molecules leave the cytoplasmic/exoplasmic leaflet, enter the cytoplasmic/exoplasmic leaflet, and then return to its original leaflet[49]. The frequency of cholesterol flip-flop is calculated as $\frac{number\ of\ cholesterol\ molecules\ flipping}{time}$, with time in μs.

Density Analysis. The number density of CG beads in the pure EL, pure CL, and mid-zone is calculated using the MDAnalysis library. The density profile is approximated by discretizing the simulation box into areas of 1nm×1nm and calculating the local number density in each region.

Results and Discussion

Plasma membrane lipid families display unique mixing affinities for other lipid species. The physiochemical properties of the RBC membrane were evaluated based on lipid-lipid interactions among the different lipid families throughout the 5 μs simulation. The lateral assembly of a lipid within the family (self-association) or with other lipid families (co-localization) was determined by mixing parameter analysis. It is concluded that the SM and PC families, key lipids in the RBC membrane's EL, exhibit a heterogeneous lipid distribution. The SM lipids tend to self-associate and co-localize with cholesterol to form nanodomains (Figure

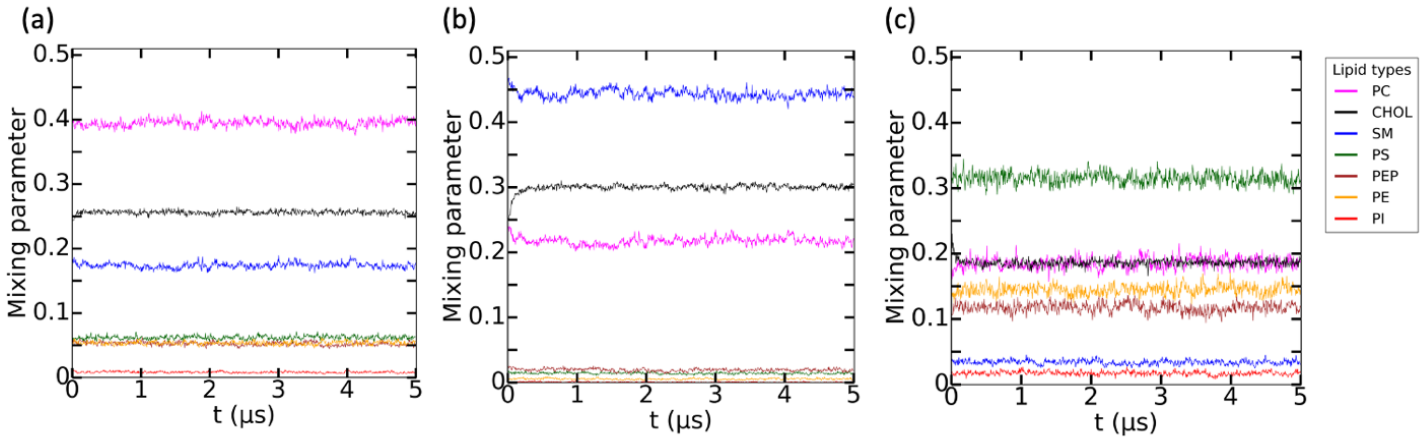

Figure 5. RBC plasma membrane plots for mixing parameter percents over time in μs. (a) PC as the reference lipid, (b) SM and the reference lipid, and (c) PS as the reference lipid

5a). These nanodomains do not extend more than 3-4 nm and are separated by PC lipids. The SM's tendency to form nanodomains is supported by the visualization of the mixing parameters (Figure 6a). SM lipids have the highest proportion of self-association (46%) followed by a mixing affinity with cholesterol (30%) and PC (22%). The other lipid families collectively represent <3% mixing. The SM concentration in the CL in negligible to form clusters. The PC lipids self-associate to a lesser extent than the SM (Figure 5b). As a result, the PC lipids in the EL fill the area not occupied by the SM nanodomains leading to some local clustering. The PC clustering in the CL is characteristically distinct from the EL; here the PC lipids are much more dispersed due to the lack of SM nanodomains in the CL and lower mole fraction. The remaining lipid families in the EL have a less significant contribution to the exterior surface of the RBC. The negatively charged PS lipids have a self-associating affinity, but their clustering is not continuous to form domains. The PS lipids have almost equal mixing with PC, PE, and PEP lipids as indicted by the mixing parameter plot (Figure 5c). The highly charged PI lipids have been a focus of several computational studies[75-76]. The PI lipids are in tiny mole fractions in both leaflets and do not exhibit colocalization with any lipid family. A few examples of PI clusters in

the membrane protein interface have been reported[77-78]. The PE lipids are heterogeneously distributed in the CL with minimal self-association or clustering. The PE molecules do not exhibit affinity to any specific lipid family in the CL. The PEP is a subclass of the PE lipid that shares the same headgroup but has a vinyl ether linkage for one of its carbon chains. Like other PE lipids, the PEP lipids are found only in the CL. The mixing parameters for PEP mimic the PE lipid properties. These results display that human RBC plasma membrane leaflets have very distinct surface properties. The EL has distinct SM nanodomains while the CL has a near random distribution of PS, PE, and PEP lipid families. The remainder of the mixing parameter plots can be found in Figure A2.

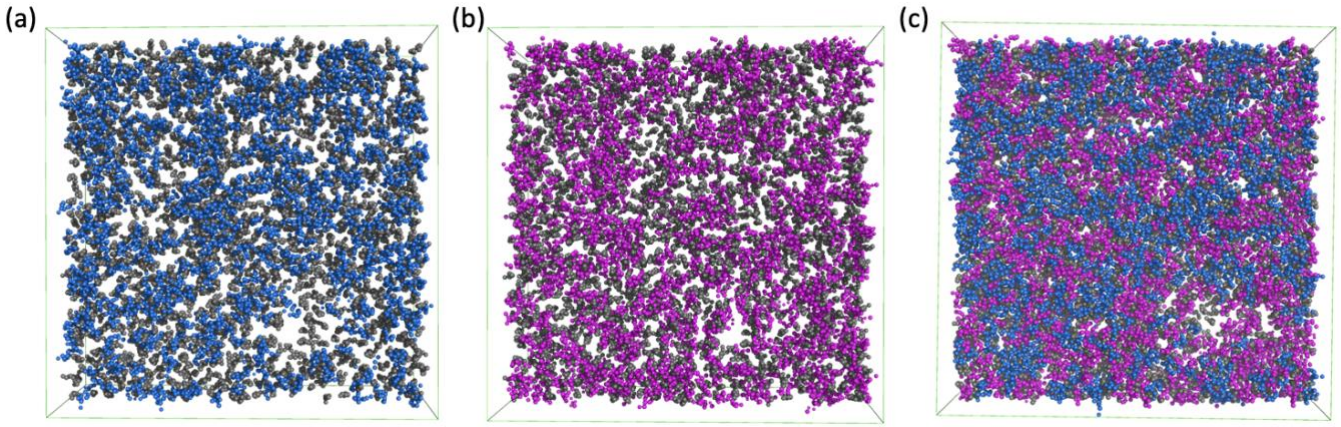

Figure 6. Top view of RBC plasma membrane displaying aggregation of SM (blue), PC (pink), and cholesterol (grey) lipids after 5 μs of simulation. (a) Nanodomain formation of SM with cholesterol, (b) Nanodomain formation of PC with cholesterol, and (c) Mixing of SM, PC, and cholesterol lipids.

Lipid order parameters influence the bilayer assembly of the EL and CL. Membrane asymmetry is reflected in terms of membrane composition. Comparing lipid orders in the EL and Cl is another approach to show lipid packing in this asymmetry RBC plasma membrane. The order parameter, S_{CD}, was generated for the acyl chain beads for each lipid. Within each leaflet, the cumulative S_{CD} was calculated from the same set of carbon beads (Figure 7). The S_{CD} decreases as the acyl chain beads of interest move from headgroups towards lipid tails, meaning

the farther the carbon bead is location away from the headgroups, the less ordered it becomes. This trend holds true for both leaflets. Overall, the EL has a larger S_{CD} and contains more ordered lipids than the CL, which is consistent with the latest reports[25,49]. After analyzing order parameters from the perspective of position of the carbon beads, the order parameter of each acyl chain in the lipid molecules was calculated (Table 2). It is evident from the order parameters that saturated and unsaturated acyl chains have remarkably different contributions to a lipid's shape and packing in the membrane (Figure A1). The box plots of notable lipids are shown in Figure A6. For example, PAPC's 16:0 acyl chain is much more ordered (0.52±0.258) than the 20:4 (0.13±0.214) chain. All the SM family lipids exhibit differences in the lipid order of their two acyl chains. There is a remarkable disparity in the median values of the PUPE lipid's order parameters; the shorter, saturated (16:0) chain is ordered (0.41±0.281), while the longer, unsaturated chain (22:6) is disordered (0.04±0.196). The PEP1 and PEP2 acyl chains also show differences in the vinyl ester linked chain versus the ether linked acyl chain. Interestingly, the saturated DPPC lipid (16:0-16:0), sequestered in the CL in the plasma membrane, has high order parameters (0.46±0.274 and 0.49±0.272) for both acyl chains. The statistical analysis of the lipid order parameters highlights three important aspects: (a) on average the El lipids are more ordered than the CL lipids; (b) this unbalanced order of lipids between the leaflets is relative to the packing of lipids in each leaflet; (c) between the two acyl chains of a lipid, the shorter and

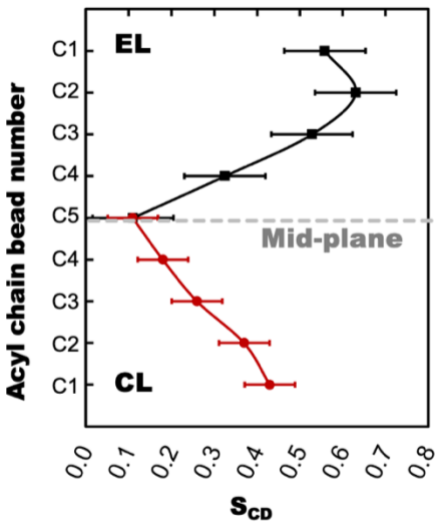

Figure 7. S_{CD} by carbon Bead. Order parameters of all lipids in EL (black) and the CL (red), excluding cholesterol lipids. The dashed lines (grey) indicate the mid-plane of the bilayer where one leaflet ends and the other begins.

Table 2. Lipid order parameters (S_{CD}) separated by exoplasmic and cytoplasmic leaflets and fatty acid tail.

Lipid	Acyl chain	Exoplasmic Leaflet		Cytoplasmic Leaflet	
		Tail 1 *Mean* S_{CD}	*Tail 2* *Mean* S_{CD}	*Tail 1* *Mean* S_{CD}	*Tail 2* *Mean* S_{CD}
PNSM	42:2;2	0.47±0.187	0.71±0.259	—	—
PLSM	42:1;2	0.51±0.215	0.70±0.265	—	—
PAPC	16:0-20:4	0.52±0.258	0.13±0.214	—	—
POPC	18:0-18:1	0.55±0.252	0.47±0.257	—	—
DPSM	34:1;2	0.63±0.221	0.71±0.256	0.44±0.277	0.30±0.348
PIPC	16:0-18:2	0.53±0.255	0.26±0.267	0.42±0.280	0.21±0.249
PAPS	18:0-20:4	0.52±0.250	0.29±0.326	0.42±0.278	0.11±0.204
PEP1	18:1-20:4	0.38±0.265	0.14±0.218	0.30±0.265	0.11±0.202
POPE	16:0-18:1	—	—	0.41±0.280	0.34±0.264
PUPE	16:0-22:6	—	—	0.41±0.281	0.04±0.196
PEPE	18:1-20:4	—	—	0.31±0.264	0.11±0.203
PEP2	18:2-20:4	—	—	0.20±0.244	0.11±0.207
DPPC	16:0-16:0	—	—	0.46±0.274	0.49±0.272
POPC	16:0-18:1	—	—	0.42±0.280	0.35±0.262
PAPS2	18:0-20:4	—	—	0.40±0.280	0.10±0.201
PIP2	18:1-20:4	—	—	0.32±0.259	0.13±0.199

saturated chain is more ordered than the longer, unsaturated acyl chains. The pairing of short/long, saturated/unsaturated, and charged/zwitterionc lipids along with asymmetric lipid compositions of the leaflets is critical in the lipid assembly into a bilayer that ultimately results in unique biophysical properties of the plasma membrane.

Cholesterol lipids flip between leaflets with preference for the EL. Several simulation studies have focused on evaluating the interaction of cholesterol with the lipids and the flip-flop dynamics between the membrane leaflets. Analyzing this dynamic behavior of cholesterol is experimentally challenging due to multiple confounding factors[46,79-80]. The use of computational tools can capture the cholesterol flip-flop dynamics[43-45,47-49]. In the initial system set-up, cholesterol was distributed equally in each leaflet. In the pre-equilibrium NVT and NPT stages of the simulation, more molecules of cholesterol flipped from the CL to the EL than vice-versa.

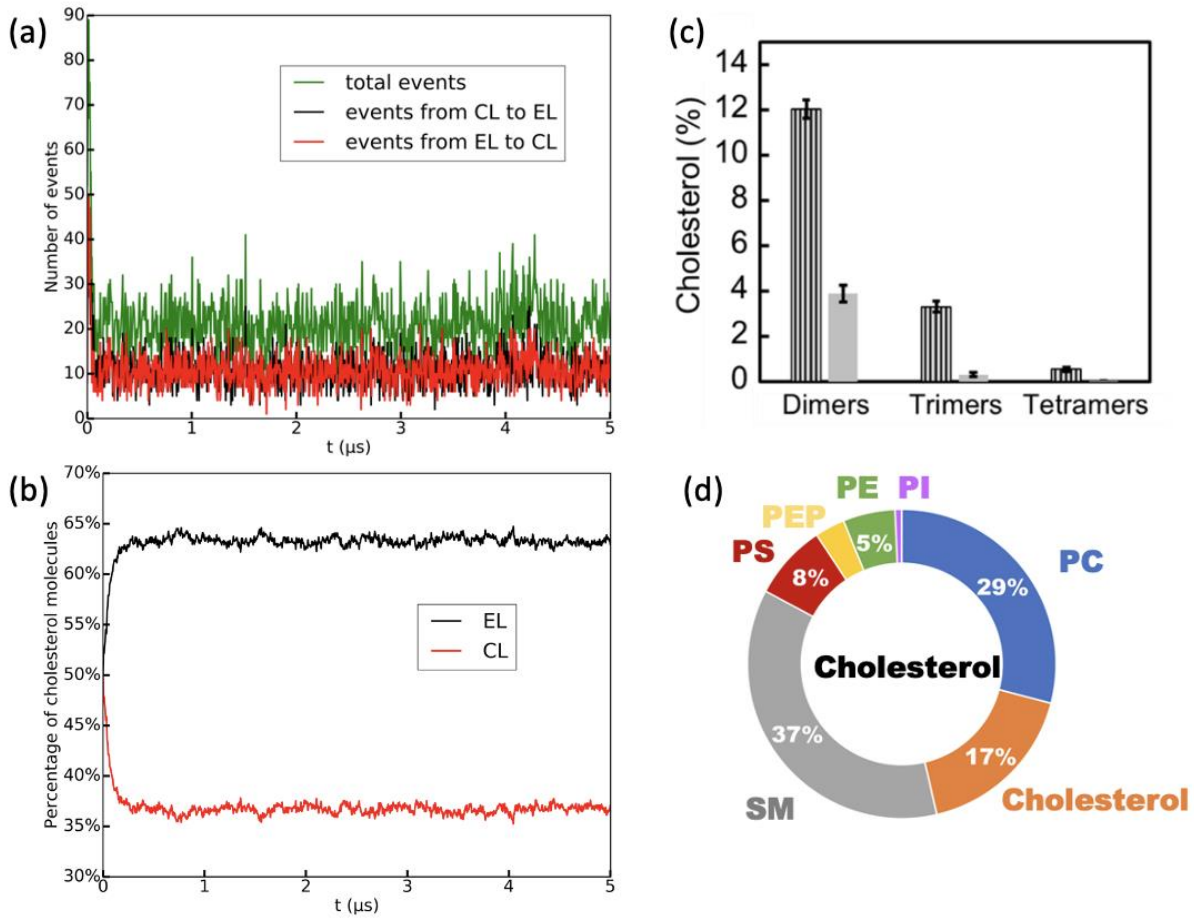

Figure 8. Quantitative analysis of cholesterol partitioning in the RBC membrane. (a) Number of cholesterol flips from CL to EL (back), from EL to CL (red), and the total number of flip-flops (green) as a function of simulation time. (b) Percent cholesterols in EL (black) and in CL (red) over the five microseconds. (c) Bar plot of cholesterol oligomers (%) in the form of dimers, trimers, or tetramers in the EL (vertical lines) versus CL (solid) at equilibrium. (d) Mixing parameters of cholesterol with other lipid families.

At equilibrium, the rate of cholesterol flip-flop between the two leaflets reached a stable distribution (Figure 8a and 8b); the EL and CL cholesterol distribution is 64±3% and 36±3%, respectively. Although a vast majority of the cholesterol molecules are solitary, some dimers, trimers, and tetramers were observed (Figure 8c). The cholesterol oligomers were prevalent in the EL (16%) compared to the CL (4%). The oligomerization of cholesterol in the EL can be explained by the higher cholesterol concentration and the affinity to colocalize with the SM lipids. The cholesterol dimers have weak interactions with a short residence time of 5-10 ns. The presence of cholesterol oligomers was confirmed in a recent study in which model phospholipid

membranes were probed with solid-state nuclear magnetic resonance (NMR) spectroscopy[81]. Previous experimental and computational studies have demonstrated the preferred interaction of cholesterol with the saturated lipids[78]. It has been suggested that the interaction between cholesterol molecules and SM lipids lead to the formation of lipid domains[82-83]. The lipid mixing parameters revealed the lateral association of cholesterol with membrane lipids: SM (37%), PC (29%), cholesterol (17%), PS (8%), PE (5%), PEP (3%), and PI (1%), as shown in Figure 8d. The preferential association of cholesterol with the SM and PC lipids is established within the first few microseconds of the simulations and remains unchanged after equilibration. The triplicate simulation runs show the same cholesterol lipid mixing trends. Thus, cholesterol localization occurs disproportionately in the SM-enriched EL.

Conclusions

This research reports a detailed molecular description of the human RBC plasma membrane that replicates the experimentally determined lipid composition of each of the two asymmetric membrane leaflets. The mixing parameter, order parameter, and cholesterol flip-flop results provide evidence for the consequences of membrane asymmetry on the plasma membrane structure and its physiochemical properties. Cholesterol oligomerizes into short-lived dimers, trimers, and tetramers in the exoplasmic leaflet. The SM lipids and cholesterol laterally associate to form nanodomains in the exoplasmic leaflet. In contrast, the cytoplasmic leaflet has a near-random distribution of the PC, PS, PE, and PEP families. Excluding cholesterol, all lipid families have the highest mixing parameter with the lipids of their species. It was concluded that cholesterol lipids have an affinity for SM and PC lipids, where there are more of these in the EL than the CL. This supports the cholesterol flip-flop results that display a bias of cholesterol to flip towards the EL. Since both leaflets in the simulation have the same area, as the EL

accumulates more cholesterol, it must accommodate more lipids per area than the CL. This leads to the EL being more densely packed than the CL. In addition, cholesterol has a planar structure and prefers to orient itself between saturated tails. The results display that the EL is overall more saturated than the CL, which provides another aspect that attracts cholesterol to the EL. The physiochemical properties of this realistic RBC membrane model can be applicable to protein assembly simulations. Due to the high density of the EL, RBC plasma membrane proteins tend to have longer and thinner transmembrane domains (TMDs) in the thicker, saturated, and more tightly packed leaflet. Therefore, the biophysical plasma membrane asymmetry of the red blood cell is attributed to the CL containing more unsaturations per lipid than the EL due to the vast difference in their lipid species compositions. Fingerprinting the plasma membrane lipidome is pivotal in elucidating how cells exchange metabolites, transfer signals, and facilitate protein assembly.

CHAPTER II – Utilizing CLASP for antibiotic screening of *P. aeruginosa* porins

Introduction

Antibiotic Resistance. Since the discovery and subsequent research of antibiotics in the early 20th century, scientists have developed over 100 types of antibiotics to fight infections of a vast range of bacteria. However, in recent years, these antibiotics are decreasing in effectiveness in treating common infections. This ineffectiveness can be attributed to the excessive use of antibiotics in hospitals and agriculture of developed, high-income countries causing selection pressure for resistant strains of bacteria to strive[84]. Bacterial antibiotic resistance is a consequence of mutations in microbes to provide a competitive advantage for these mutated

strains in the environment[84]. Examples of resistant bacteria include meticillin-resistant, gram-positive *Staphylococcus aureus* (MRSA) USA 300 and *Escherichia coli* ST131 and are becoming even more prevalent among diagnosed bacterial infections. The spread of these resistant bacteria can be attributed to interspecies gene transmission, poor sanitation and hygiene in communities and hospitals, and the consistent increase in global disease transmission. Epidemiology research has displayed the ease at which this resistance can spread worldwide with antibiotic-resistant gonorrhea surfacing in Vietnam in 1967 spreading to the Philippines and ultimately to the United States. In addition, even synthetic antibiotics, such as Quinolone, have become ineffective in the 30 years since its inception and this resistance has been connected to the evolution of hospital MRSA[84]. In the past 75 years since antibiotics were introduced, almost all disease-causing bacteria have become resistant to the antibiotics that treat them. This trend can be observed in the β-lactamases antibiotic class with a 10-fold increase in resistant β-lactamases since 1990. β-lactam antibiotics in Gram-negative bacteria have been the focus of critical research for battling antibiotic resistance. Specifically, *Pseudomonas aeruginosa*, *Acinetobacter baumannii* and *Klebsiella pneumoniae* are Gram-negative bacteria that have evolved into multi-drug resistant (MDR) pathogens[85], bacteria that are resistant to three or more classes of antibiotics.

Pseudomonas aeruginosa. Pseudomonas aeruginosa is a Gram-negative bacterium that is at the forefront of hospital environment infections. This bacterium is the cause of 17% of healthcare-associated pneumonia and is the seventh most common organism found in bloodstream infections[85]. The *P. aeruginosa* species includes numerous β-lactam resistance determinants: efflux pumps (mexAB), porin mutations (OprD), inducible AmpC β-lactamases, extended spectrum (PER and OXA) and metallo- β-lactamases (IMP and VIM), and biofilm production. β-lactams are inhibited from penetrating *P. aeruginosa* cell via the resistance-nodulation-cell division (RND) family of efflux pumps. These pumps work with periplasmic membrane fusion proteins and outer membrane efflux proteins to span both cell membranes to extrude antibiotics from the cytoplasm and periplasmic space. Specifically, with an increased expression of the MexAB-OprM multi-drug efflux pump, the more resistant the bacterium is towards targeted antibiotics. *P. aeruginosa* has evolved resistance to most antibiotics except for imipenem, since it is not extruded from the bacteria itself and does not possess RND efflux pumps. This low susceptibility to efflux has allowed imipenem to remain an effective candidate against *P. aeruginosa*. Imipenem enters the bacterial cell via the OprD2 porin which presence decreased because of drug pressure[85]. Moreover, the loss of this porin is caused by significant novel

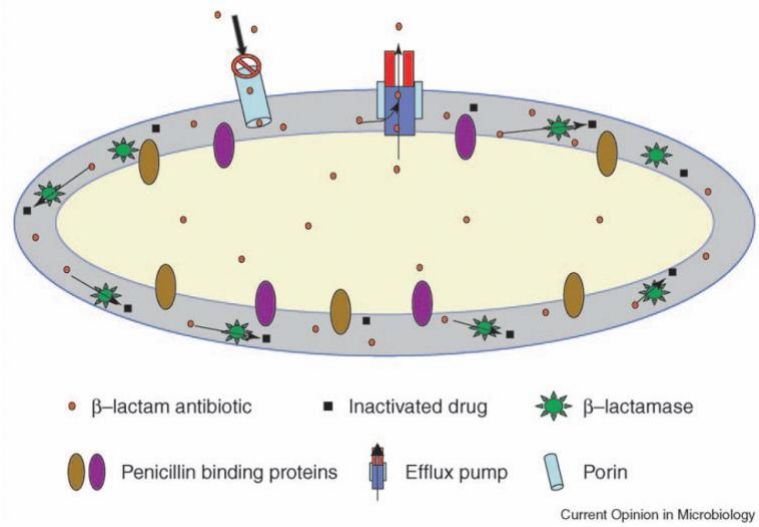

Figure 9. Resistance mechanisms interactions to β-lactam antibiotics in the Gram-negative bacterial cell[85].

insertion sequences interrupting the expression of the OprD2 porin, providing a decrease in channels by which antibiotics can enter through.

Table 3[85]. *P. aeruginosa* Porins and their respective PDB IDS and known antibiotic transport.

Porin	Antibiotic Transport	PDB ID
OccD1	Imipenem/meropenem	3SY7
OccK1	Carbenicillin, cefoxitin, tetracycline, temocillin	3SYS
OccK2	Carbenicillin, cefoxitin, gentamycin, temocillin	3SZD
OccK3	Cefotaxime	3SZV
OccK7	Meropenem	4FRT

The *P. aeruginosa* outer membrane contains porins that are passive transporters of water-soluble molecules (600-700 Da)[86]. These porins fold in the outer membrane as β-barrels comprised of antiparallel β-sheets with hydrophobic amino acid residues facing outward and hydrophilic residues facing inward, lining the constricted pore[87]. The OprF is the major outer membrane porin that performs structural, adhesion, and signaling functions. Other porins include OprB and OprB2 responsible for glucose diffusion, OprG and OprH (small outer membrane proteins), OprP and OprO responsible for phosphate/pyrophosphate uptake. There are nineteen additional proteins in the OprD (Occ) family that are separated into two subfamilies; 8 porins in the OccD family and 11 porins in the OccK family[87]. The antibiotic transport for each known *P. aeruginosa* porin and their respective possible functions are outlined in Table 3.

Experimental Overview. This work aims to computationally prepare the eight OccK porins and six possible antibiotic candidates for use in the Computational Antibiotic Screening Platform (CLASP[88]). CLASP can produce comprehensive thermodynamic and kinetic output data at a fast rate, to make drug screening more efficient. The preparation of these proteins and molecules is critical for the success of CLASP because the structures need to be translated into the CG resolution for the simulation to run in the optimal computational timescale and length. Once the porin and antibiotic inputs are prepared, the CLASP protocol (Figure 10) can be executed which will produce a trajectory of the antibiotic through the porin channel. The output files are analyzed by producing a free energy profile of the potential mean force (PMF) of the antibiotic molecule transport from the extracellular to the periplasmic space, the permeation barrier of the molecule, the orientational analysis of the molecule, and the contact analysis of the molecule with the protein residues in the porin channel.

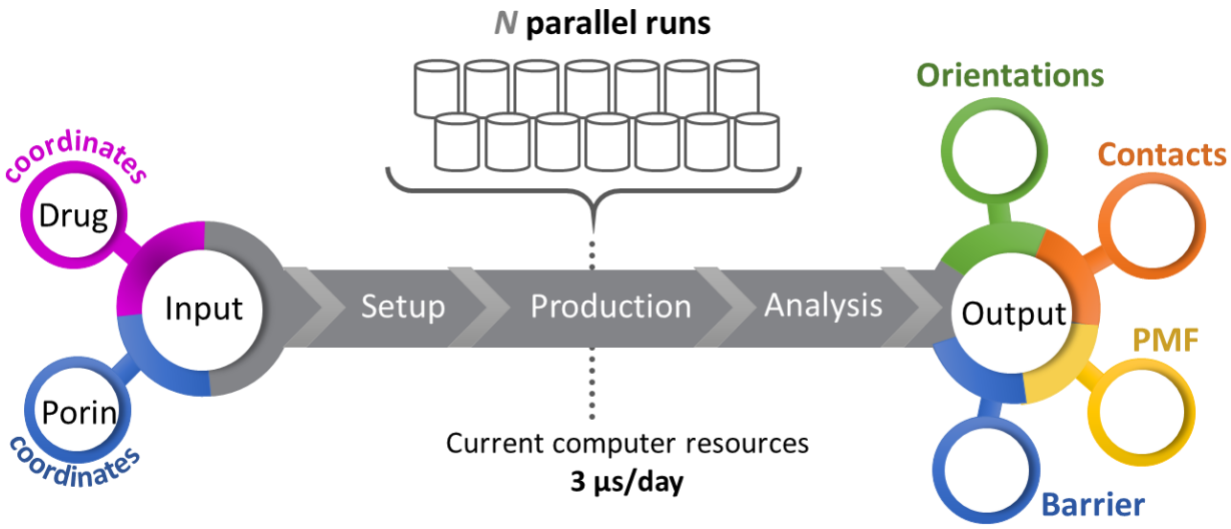

Figure 10. The CLASP workflow. The systematic representation of CLASP inputs and outputs. The porin and solute coordinates are the required inputs, which then are processed to generate *N* parallel umbrella sampling runs. The post simulation analysis scripts combine the *N* trajectories to generate the free energy profile, solute-protein residue contact map, and solute orientational analysis[88].

Methods

Porin Preparation. The x-ray crystallographic porin structures for OccK1-OccK8 were obtained from the RCSB Protein Data Bank (PDB); the porin IDs are listed in Table 3. These porins were centered within the periodic boundary condition (PBC) box before performing homology modeling. Homology modeling, also known as comparative modeling, constructs an atomistic-resolution model of the protein from the provided amino acid sequence (Figure 11). The homology modeling software YASARA[89] was utilized by providing the PDB structure as the query sequence which is used in conjunction with an alignment that maps the remaining residues to produce a homologue of more known protein structures. Moreover, the software acknowledges gaps in the residue sequence of the input structure and fills the gaps based on known protein structures. Then the structures were optimized in the atomistic resolution using the CHARMM36 force field[90]. The structures then underwent equilibration in the isothermal-isochoric (NVT) and isothermal-isobaric (NPT) conditions where the output of the NPT is the starting input structure for CLASP. Both the NVT and NPT simulations were conducted for 200 ns each at T = 320 K. The point mutations of each porin structure were generated by the CHARMM-GUI open-source webserver and these mutated structures were optimized as well. The output porin structures were coarse grained using the *martinize.py* script with MARTINIlv2.1 force field parameter[56] to maintain the porin's secondary structure[88].

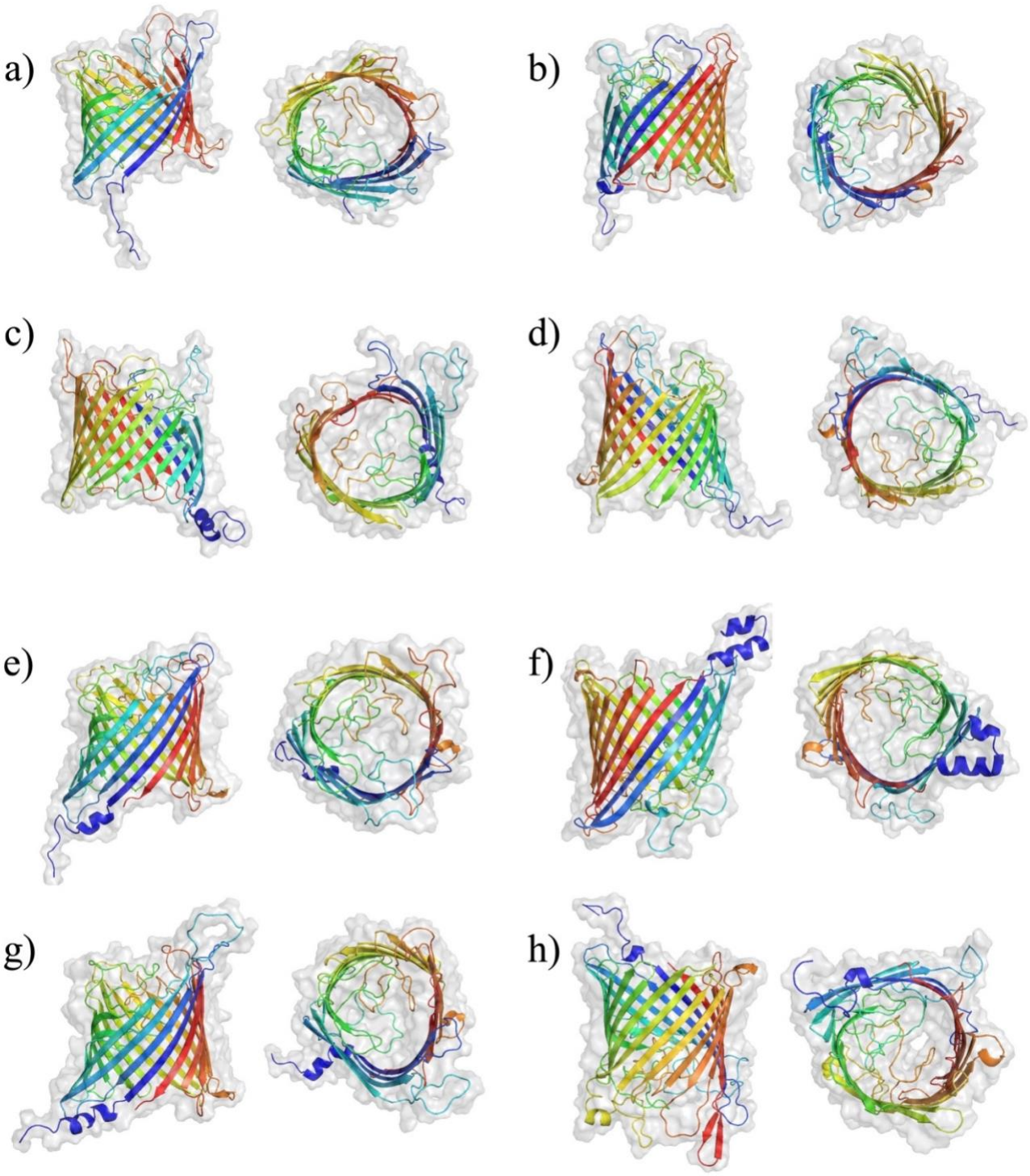

Figure 11. Homology modeled *P. aeruginosa* porin structures displayed in front and top view. (a) OccK1, (b) OccK2, (c) OccK3, (d) OccK4, (e) OccK5, (f) OccK6, (g) OccK7, and (h) OccK8. The porin surface is also displayed as a transparent shadow.

Porin-Membrane System. Each CG porin was separately embedded (along the z-axis) into an asymmetrical 10 × 10 nm^2 (in the xy-plane) patch of *P. aeruginosa* membrane using the *BOB.py* script; Bacterial Outermembrane Builder[58,91], a modified *insane.py* script with CG parameters for bacterial outer membranes. The exoplasmic leaflet of the membrane patch is comprised of *P.* aeruginosa lipid A and 1,2-dipalmitoyl-sn-glycero-3-phosphoethanolamine (DPPE) in a 9:1 ratio. The periplasmic leaflet contained pure DPPE. The porin-membrane system was placed in a 10 × 10 × 12 nm^3 simulation box and was solvated with standard MARTINI water (9:1 of W:WF) and 150 mM $CaCl_2$.

Antibiotic Coarse Grain Preparation. Carbenicillin, Cefoxitin, Cefotaxime, and Temocillin were prepared using PyCGTOOL[92], a python script that generates CG model parameters for the

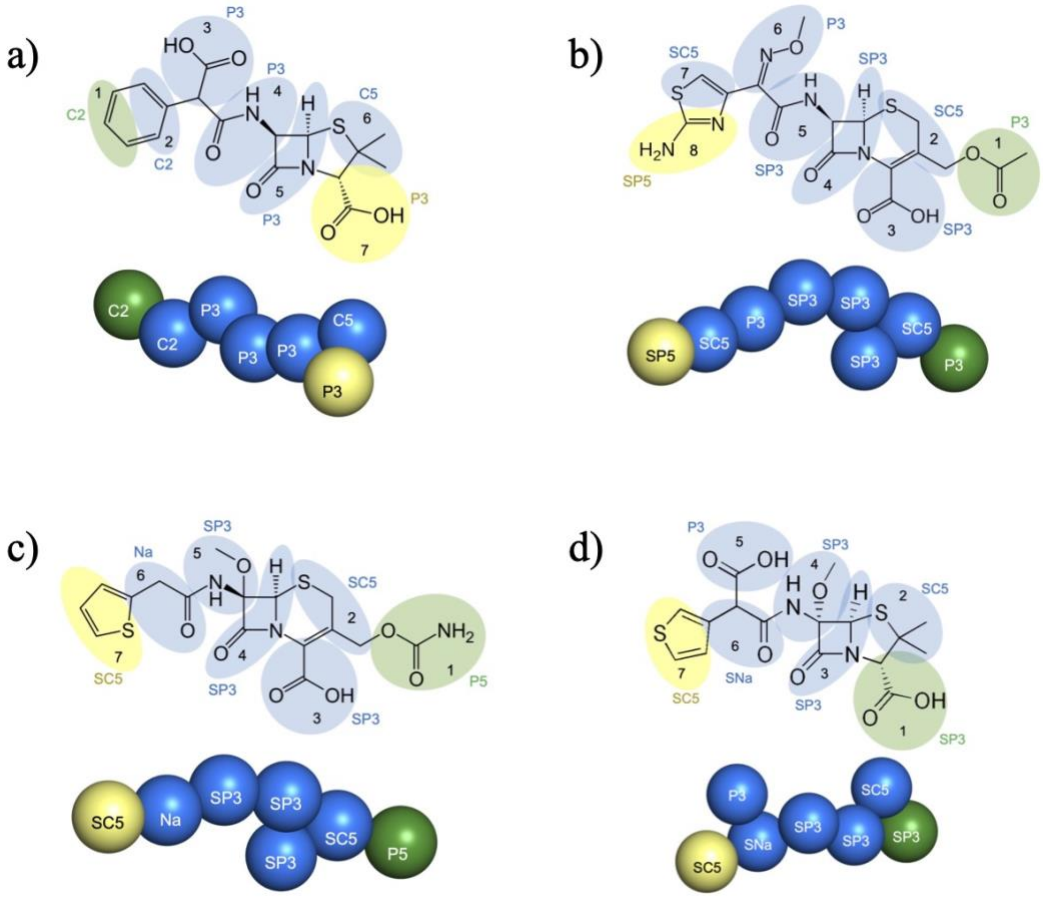

Figure 12. Antibiotic CG mapping. (a) Carbenicillin, (b) Cefotaxime, (c) Cefoxitin, and (d) Temocillin. Green beads denote the first bead of the molecule, and the yellow bead denotes the last bead.

molecule based on its respective atomistic dynamical data[88]. This script provides molecular topologies and CG parameters to the inputted atomistic structure of the antibiotic. The CG mappings of the four antibiotic molecules are displayed in Figure 12. The molecules were coarse grained based on MARTINI CG[93] which recommends mapping four adjoining nonhydrogen atoms into one CG bead which will preserve bonded and nonbonded interactions of the atomistic level.

CG MD Simulation. Using GROMACS 5.12[71], the porin-membrane system was energy minimized using the steepest-decent algorithm[88] until the maximum force on any bead was below the tolerance parameter of 10 $kJmol^{-1}nm^{-1}$. Then NVT and NPT equilibration was conducted for 0.02 μs and 2 μs, respectively. A 20 fs time step was used for the equilibration and production simulations with a temperature of 320 K for all systems using the v-rescale thermostat with $\tau t = 1$ ps. A semi-isotropic pressure coupling of 1 bar was maintained using Parrinello-Rahman barostat[73] with $\tau p = 4$ ps. Both the nonbonded van der Waals and the electrostatic interaction cut-offs were set to 1.2 nm and periodic boundary conditions were applied in all three dimensions.

CLASP. CLASP was performed to generate $N = 400$ separate folders (US windows), each with a substrate molecule of a unique location defined within its free energy profile. The molecule's permeation coordinate (s) is parallel to the z-axis and the length of the protein channel from the extracellular to periplasmic region along s is termed L_s (Figure 13). The free energy profile along s is generated by dividing L_s into N umbrella sampling windows (W_i) with uniform spacing of L_s/N nm[88]. The antibiotic molecule is inserted into each W_i window and the insertion coordinates are calculated relative to the porin's center-of-mass (COM). The porins contain a constriction zone within the channel forming an hourglass shape, therefore the COM can be

found in the middle of the porin. The COM location is accepted as $W_{N/2}$, where there is an equal number of windows above and below the COM. Each of the US folders were equipped with input files and python scripts to perform energy minimization and US simulations independently. All N simulation jobs run synchronously in separate computer cluster nodes to promote maximum efficiency and fast completion time.

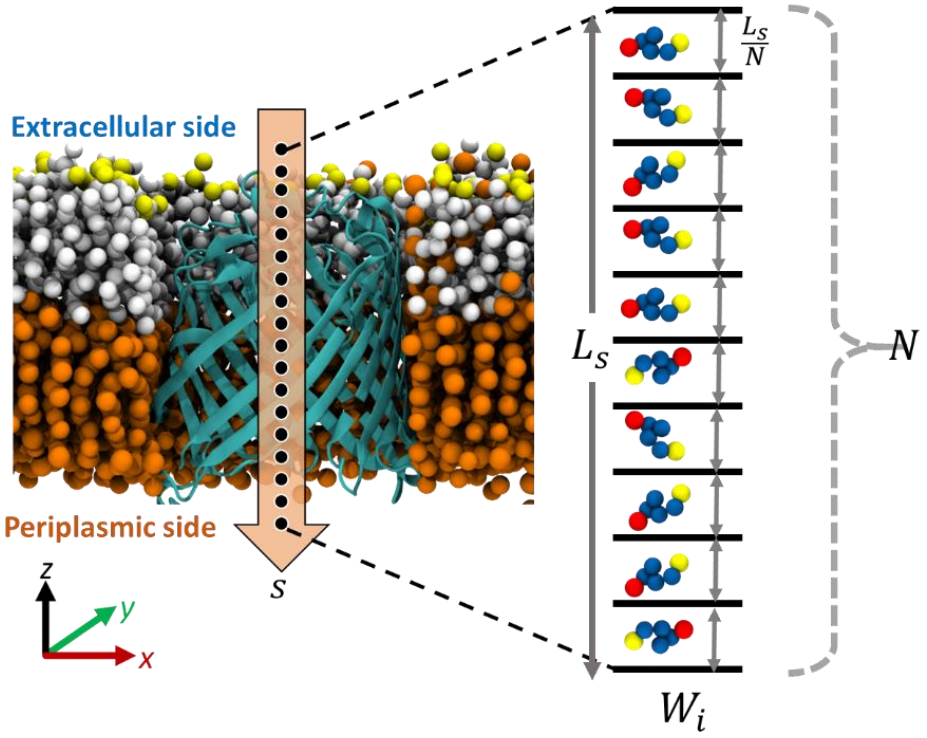

Figure 13. CLASP simulation setup. The membrane embedded porin channel oriented parallel to the z-axis is divided into N equidistant umbrella sampling windows. The probe molecule is inserted into each W_i window[88].

Free Energy Profile Analysis. The free energy profile of the antibiotic molecule's transport from the extracellular to the periplasmic region is computed as the potential of mean force (PMF) along the s path. The starting structure, molecular topology, the simulation parameters, and other data files from the CLASP simulation can be used as inputs for the GROMACS *wham* commands to generate a plottable PMF file. Arginine was used an appropriate control due to its small size and +1 charge, that was translated to three CG beads, which is significantly smaller than the seven to eight CG beads of the antibiotic molecules. Glycine, with a charge of 0 and 1

CG bead, and glutamate, with a charge of -1 and 2 CG beads are also being explored as controls for CLASP to cover a range of charges and beads sizes.

Histogram Analysis. Another output graphable file generated from the same procedure as the PMF is the Histogram. The Histogram contains different colored bars of varying heights that represent the sampling of a single US window. The overlap of the bases of these bars is of importance to display the continuous sampling from one window the next, forming a cohesive trajectory of the solute molecule through the porin (Figure 17b).

Contact Analysis. As the solute molecule travels through the porin it interacts with protein residues lining the channels. A contact is said to have occurred if the distance between any CG beads of the solute and residue is within 1.2 nm of each other. These interactions for all N windows are determined by assigning them values; 1 when formed or 0 when contact is broken. Then, the cumulative number of contacts made by the solute with each residue in the windows is calculated and sorted from smallest to largest based on the total number of residue-solute contacts. This is done to identify the highest contacting residues in the 99^{th} percentile.

Results and Discussion

The results of a simulation with the small molecule arginine traveling through the OccK1 porin of *P. aeruginosa* are displayed in Figure 14. The PMF profile of arginine displays a stabilization in energy before entering the porin and after exiting the porin, which is to be expected (Figure 14a). Once arginine moves closer to the N-terminus, the small molecule is pulled into the porin where the energy (E) experienced by the molecule increases in the channel. The spike in energy is displayed between 0 and 1 nm, which can be determined to be the bottleneck region of the porin. The contact analysis map (Figure 14c) for arginine exhibits tyrosine (Y290), arginine (R311), and phenylalanine (F318) as the protein residues with the highest contact with arginine.

This is due to the large sizes and charges that protrude into the bottleneck region causing high contact with the small molecule as it travels. In addition, the US windows 310-350 can be concluded as the bottleneck due to the high frequency of contacts, especially contacts in the 90th percentile. The high energy profile in the bottleneck region of OccK1 corresponds to the three

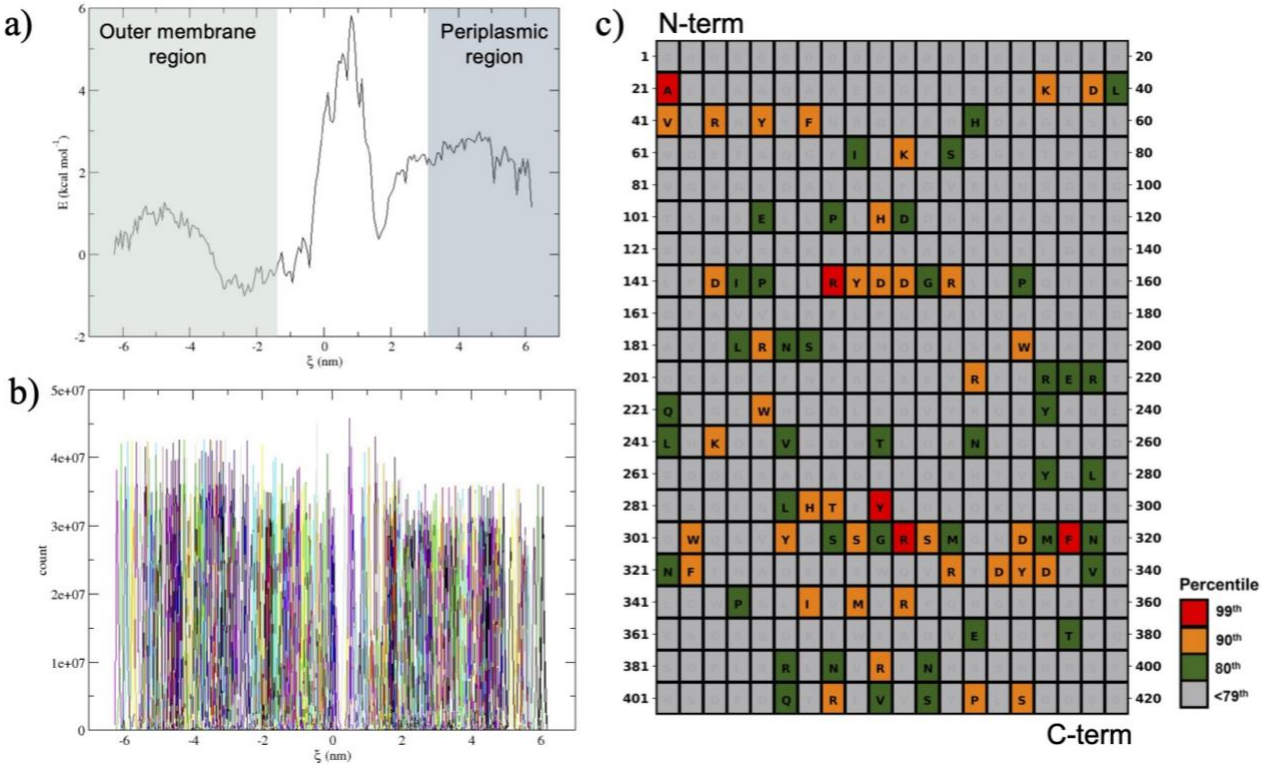

Figure 14. Small molecule arginine simulation through the OccK1 porin. (a) PMF graph displaying the energy of arginine as it proceeds through the outer membrane region (green), the constriction zone (white), and the periplasmic region (blue); (b) Simulation histogram of all US windows; (c) Contact Analysis Map where axis values correspond to the residue number in OccK1.

amino acid residues that interfere with the small molecule's trajectory. In addition, when analyzing the porin residues it can be observed that the tyrosine, arginine, and phenylalanine residues do protrude into the channel and can obstruct the trajectory of a molecule.

Conclusions and Future Work

By conducting a control experiment for the OccK1 porin of the *P. aeruginosa* porin, OccK1, a better comprehensive understanding of the channel is obtained. Since arginine is a very small molecule, the free energy of a larger molecule can be hypothesized and can be better set up for the CLASP simulation. In addition, insight into the prominent amino acid residues in the porin channel of OccK1 allows us to apply this information to subsequent antibiotic screenings for this porin. The control protocol outlined in this work can be applied to the other seven porins in the OccK family using arginine, glycine, and glutamate to establish a foundation understanding of the porin and how it interacts with molecules before testing larger, more complex molecules, such as antibiotics. This work will be continued by utilizing the prepared porins (OccK1-OccK8) and antibiotics to conduct analyses, such as the ones presented here. Once a collective profile is obtained from these simulations, it can be used to guide experimental researchers in antibiotic research and aid in the discovery of better antibiotics for antibiotic-resistant bacteria.

Appendix

Table A1. MARTINI CG beads and parameters for PLSM

Bond	R(nm)	K_{bond} (kJ mol^{-1} nm^{-2})
1-2	0.47	1250
2-3	0.47	1250
3-4	0.37	1250
3-5	0.47	1250
5-6	0.47	1250
6-7	0.47	1250
4-8	0.47	1250
8-9	0.47	1250
9-10	0.47	1250
10-11	0.47	1250
11-12	0.47	1250
12-13	0.47	1250

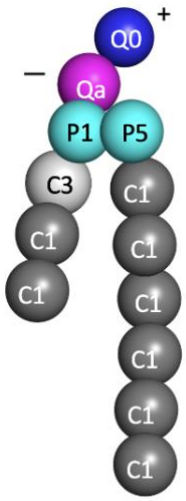

Angle	θ (deg)	K_{angle} (kJ mol^{-1})
2-3-4	120	25
2-3-5	180	25
3-5-6	180	45
5-6-7	180	25
4-8-9	180	25
8-9-10	180	25
9-10-11	180	25
10-11-12	180	25
11-12-13	180	25

Table A2. MARTINI CG beads and parameters for PEP1

Bond	R(nm)	K_{bond} (kJ mol^{-1} nm^{-2})
1-2	0.47	1250
2-3	0.47	1250
3-4	0.37	1250
3-5	0.47	1250
5-6	0.47	1250
6-7	0.47	1250
7-8	0.47	1250
8-9	0.47	1250
4-10	0.47	1250
10-11	0.47	1250
11-12	0.47	1250
12-13	0.47	1250

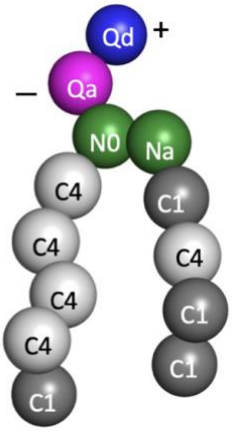

Angle	θ (deg)	K_{angle} (kJ mol^{-1})
2-3-4	120	25
2-3-5	180	25
3-5-6	100	10
5-6-7	100	10
6-7-8	100	10
7-8-9	120	45
4-10-11	180	25
10-11-12	120	45
11-12-13	180	25

Table A3. MARTINI CG beads and parameters for PEP2

Bond	R(nm)	K_{bond} (kJ mol^{-1} nm^{-2})
1-2	0.47	1250
2-3	0.47	1250
3-4	0.37	1250
3-5	0.47	1250
5-6	0.47	1250
6-7	0.47	1250
7-8	0.47	1250
8-9	0.47	1250
4-10	0.47	1250
10-11	0.47	1250
11-12	0.47	1250
12-13	0.47	1250

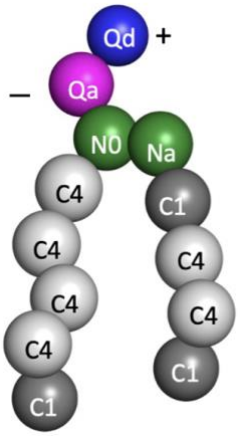

Angle	θ (deg)	K_{angle} (kJ mol^{-1})
2-3-4	120	25
2-3-5	180	25
3-5-6	100	10
5-6-7	100	10
6-7-8	100	10
7-8-9	120	45
4-10-11	180	25
10-11-12	100	10
11-12-13	120	45

Table A4. MARTINI CG beads and parameters for PEPE

Bond	R(nm)	K_{bond} (kJ mol^{-1} nm^{-2})
1-2	0.47	1250
2-3	0.47	1250
3-4	0.37	1250
3-5	0.47	1250
5-6	0.47	1250
6-7	0.47	1250
7-8	0.47	1250
8-9	0.47	1250
4-10	0.47	1250
10-11	0.47	1250
11-12	0.47	1250
12-13	0.47	1250

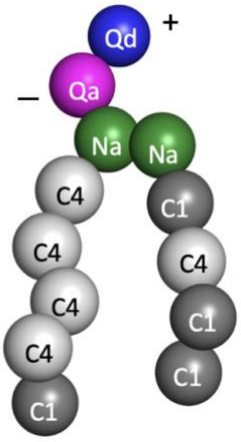

Angle	θ (deg)	K_{angle} (kJ mol^{-1})
2-3-4	120	25
2-3-5	180	25
3-5-6	100	10
5-6-7	100	10
6-7-8	100	10
7-8-9	120	45
4-10-11	180	25
10-11-12	120	45
11-12-13	180	25

Table A5. MARTINI CG beads and parameters for PIP2

Bond	R(nm)	K_{bond} (kJ mol^{-1} nm^{-2})
1-2	0.40	30000
1-3	0.40	30000
2-3	0.40	30000
2-5	0.30	25000
2-6	0.35	30000
1-5	0.40	25000
3-6	0.31	30000
5-6	0.60	25000
1-4	0.35	1250
4-7	0.47	1250
7-8	0.37	1250
7-9	0.47	1250
9-10	0.47	1250
10-11	0.47	1250
11-12	0.47	1250
12-13	0.47	1250
8-14	0.47	1250
14-15	0.47	1250
15-16	0.47	1250
16-17	0.47	1250

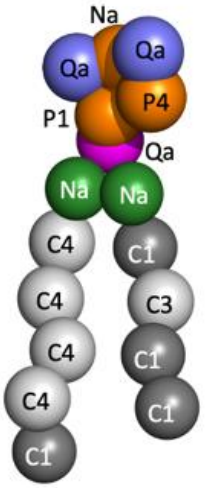

Angle	θ (deg)	K_{angle} (kJ mol^{-1})
1-4-7	140	25
7-9-10	100	10
9-10-11	100	10
10-11-12	100	10
11-12-13	125	45
8-14-15	180	25
14-15-16	120	45
15-16-17	180	25

Figure A1. Representative lipid image after 5 μs of simulation

a) PIPC, (b) DPSM, (c) PNSM, (d) PLSM, (e) POPC, (f) PAPC, (g) PAPS, (h) PEP1, (i) POPE, (j) PUPE, (k) PEPE, (l) PEP2, (m) DPPC, (n) PIP1. Coarse-grained bead types are denoted as saturated carbon (dark gray), unsaturated carbon (light gray), NC3 (dark blue), PO4 (pink), GL1 and GL2 (green), AM1 and AM2 (cyan), CNO (light blue), C1, C2, and C3 (orange), and P1 and P2 (purple).

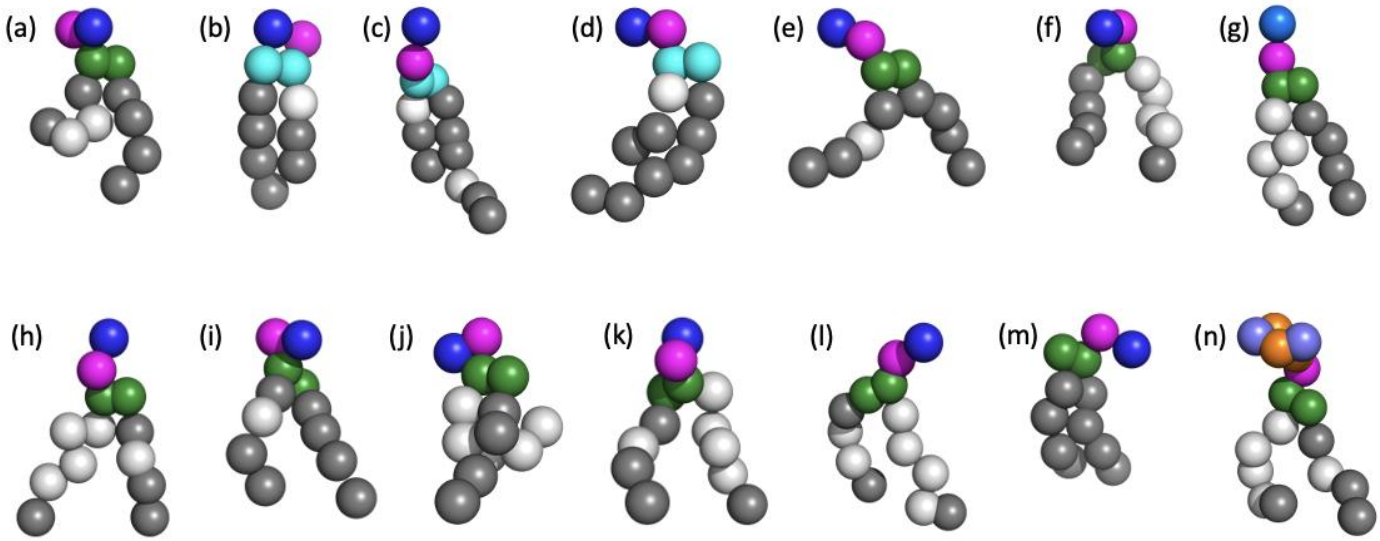

Figure A2. Mixing Parameter Plots

RBC plasma membrane plots for mixing parameter percents over time in μs. (a) cholesterol as the reference lipid, (b) PEP and the reference lipid, (c) PE as the reference lipid, and (d) PI as the reference lipid. The data is displayed as PC (pink), cholesterol (black), SM (blue), PS (green), PEP (red), PE (yellow), and PI (orange).

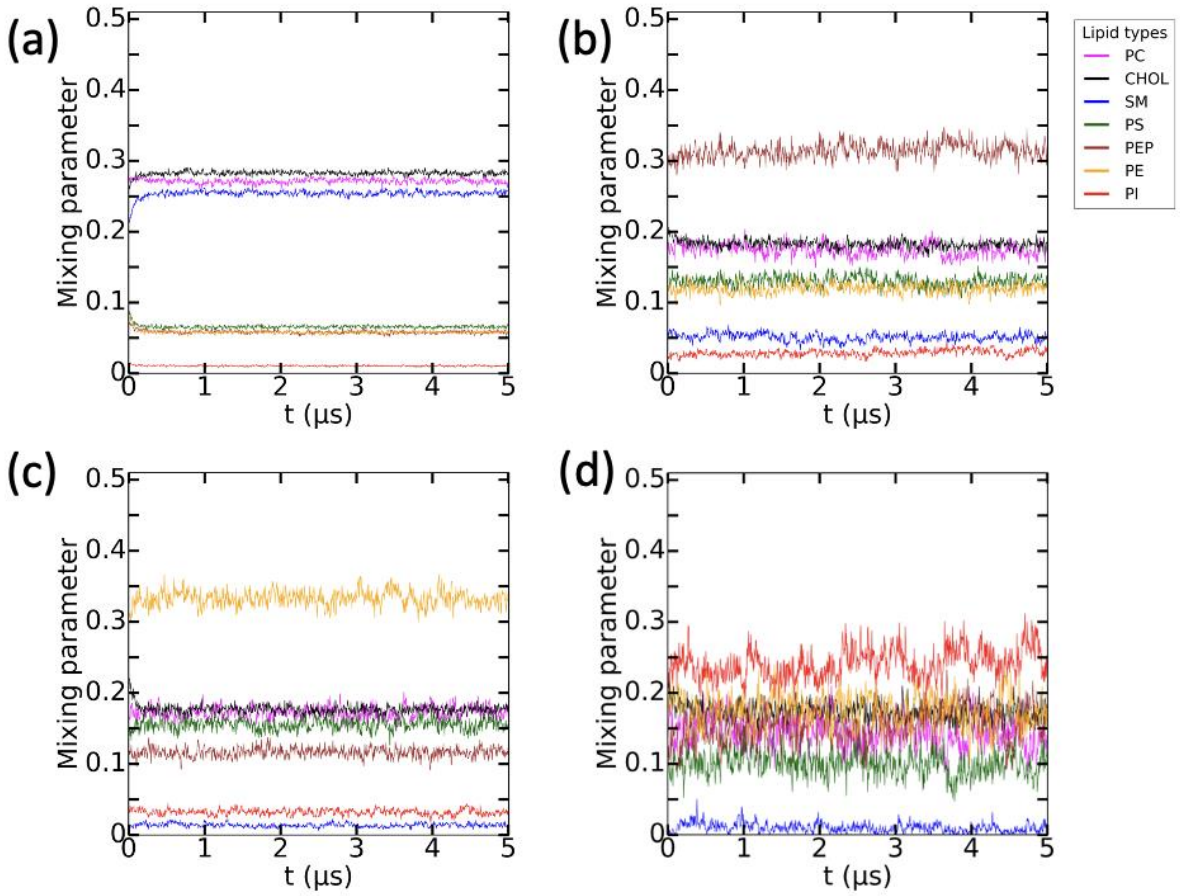

Figure A3. Order Parameters Box Plots

Order parameters of notable lipids in (a) EL and (b) CL are shown as a box-whisker plot. The two acyl chains of a lipid are distinguished by solid and striped boxes.

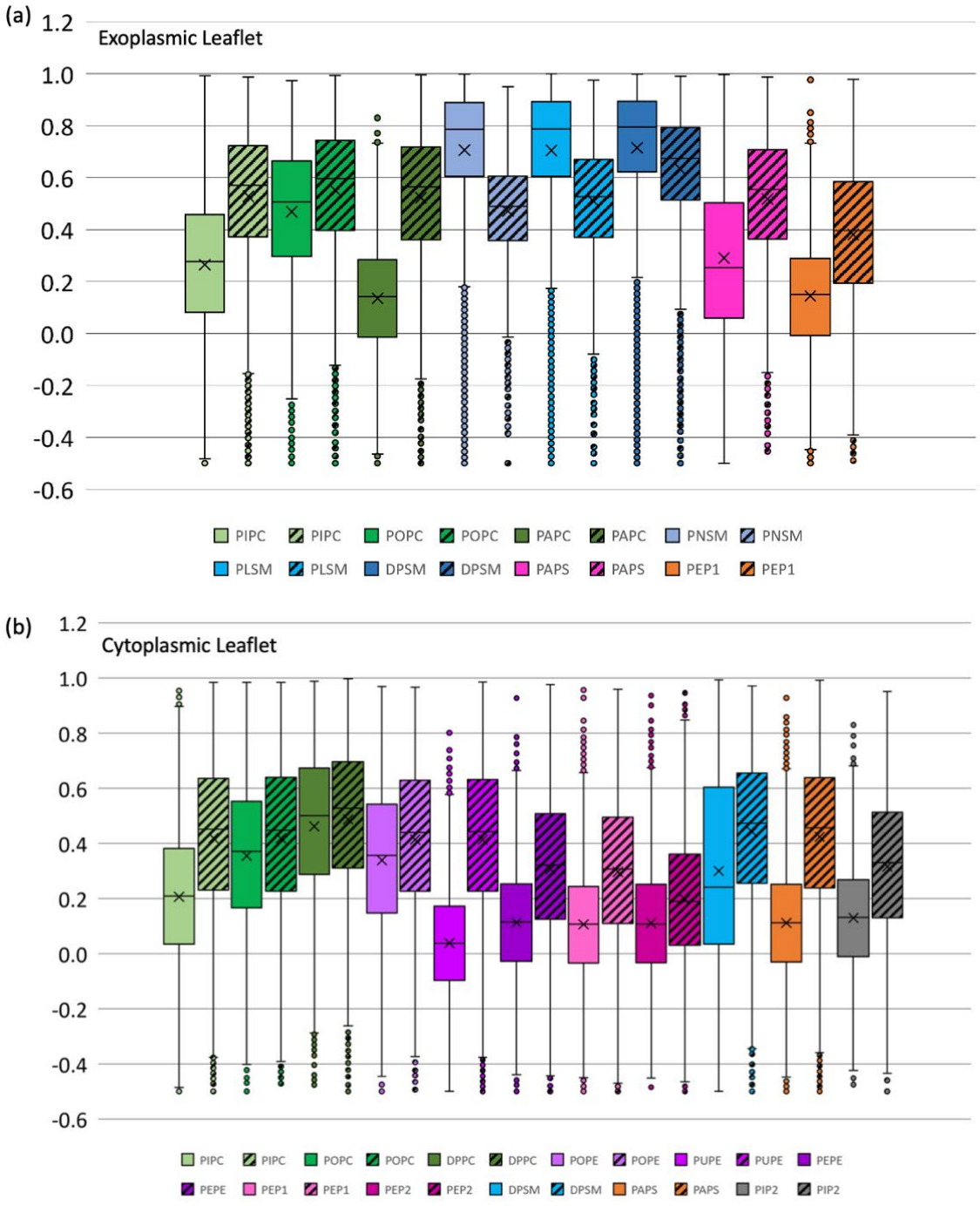

References

[1] G. Van Meer, "New EMBO Member's Review Cellular lipidomics," vol. 24, no. 18, pp. 3159–3165, 2005, doi: 10.1038/sj.emboj.7600798.

[2] T. S. Carpenter, H. Bhatia, P. Bremer, S. J. Marrink, H. I. Ingo, and F. C. Lightstone, "Computational Lipidomics of the Neuronal Plasma Membrane," *Biophys. J.*, vol. 113, pp. 2271–2280, 2017, doi: 10.1016/j.bpj.2017.10.017.

[3] Terence R. Smith, J. S., Amr El Abbadi, Divyakant Agrawal, Gustavo Alonso, Amitabh Saran. (1995). Computational modeling systems. Elsevier, 20(2), 127-153. doi:doi.org/10.1016/0306-4379(95)98558-U

[4] Weinan E, J. L. (2011). Multiscale modeling. Schloarpedia, 6, 11527. doi:10.4249/scholarpedia.11527

[5] Landau, R. H., Páez, M. J., & Bordeianu, C. C. (2008). Simulating Matter with Molecular Dynamics. In A Survey of Computational Physics (pp. 424-436): Princeton University Press.

[6] "Phospholipids," *Lumen Learning*. https://courses.lumenlearning.com/introchem/chapter/phospholipids/.

[7] D. et al. Voet, "Lipids and Biological Membranes," in *Fundamentals of Biochemistry: Life at the Molecular Level*, 4th ed., John Wiley & Sons, 2013, pp. 1–27.

[8] "Red blood cell," *Encyclopedia Britannica, Inc.*, 2020. https://www.britannica.com/science/red-blood-cell/.

[9] "Sickle cell disease," *MedlinePlus*, 2020. https://medlineplus.gov/genetics/condition/sickle-cell-disease/.

[10] J. C. McIntyre and R. G. Sleight, "Fluorescence Assay for Phospholipid Membrane Asymmetry," *Biochemistry*, vol. 30, no. 51, pp. 11819–11827, 1991, doi: 10.1021/bi00115a012.

[11] M. Ikeda, A. Kihara, and Y. Igarashi, "Lipid asymmetry of the eukaryotic plasma membrane: Functions and related enzymes," *Biol. Pharm. Bull.*, vol. 29, no. 8, pp. 1542–1546, 2006, doi: 10.1248/bpb.29.1542.

[12] A. A. Gurtovenko and I. Vattulainen, "Lipid transmembrane asymmetry and intrinsic membrane potential: Two sides of the same coin," *J. Am. Chem. Soc.*, vol. 129, no. 17, pp. 5358–5359, 2007, doi: 10.1021/ja070949m.

[13] B. Fadeel and D. Xue, “The ins and outs of phospholipid asymmetry in the plasma membrane: Roles in health and disease,” *Crit. Rev. Biochem. Mol. Biol.*, vol. 44, no. 5, pp. 264–277, 2009, doi: 10.1080/10409230903193307.

[14] P. A. Leventis and S. Grinstein, “The distribution and function of phosphatidylserine in cellular membranes,” *Annu. Rev. Biophys.*, vol. 39, no. 1, pp. 407–427, 2010, doi: 10.1146/annurev.biophys.093008.131234.

[15] R. J. Clarke, K. R. Hossain, and K. Cao, “Physiological roles of transverse lipid asymmetry of animal membranes,” *Biochim. Biophys. Acta - Biomembr.*, vol. 1862, no. 10, p. 183382, 2020, doi: 10.1016/j.bbamem.2020.183382.

[16] A. Gupta, T. Korte, A. Herrmann, and T. Wohland, “Plasma membrane asymmetry of lipid organization: Fluorescence lifetime microscopy and correlation spectroscopy analysis,” *J. Lipid Res.*, vol. 61, no. 2, pp. 252–266, 2020, doi: 10.1194/jlr.D119000364.

[17] A. S. J. Singer and G. L. Nicolson, “The Fluid Mosaic Model of the Structure of Cell Membranes Published by : American Association for the Advancement of Science Stable URL : http://www.jstor.org/stable/1733071 REFERENCES Linked references are available on JSTOR for this article : Structure,” *Science (80-.).*, vol. 175, no. 4023, pp. 720–731, 1972.

[18] T. Kusumi, A.; Nakada, C.; Ritchie, K.; Murase, K.; Suzuki, K.; Murakoshi, H.; Kasai, R. S.; Kondo, J.; Fujiwara, “Paradigm shift of the plasma membrane concept from the two-dimensional continuum fluid to the partitioned fluid: High-Speed Single-Model Tracking of Membrane Molecules,” *J. Allergy Clin. Immunol.*, vol. 130, no. 2, p. 556, 1998, [Online]. Available: http://dx.doi.org/10.1016/j.jaci.2012.05.050.

[19] S. Ilangumaran, B. Borisch, and D. C. Hoessli, “Signal Transduction via CD44: Role of Plasma Membrane Microdomains,” *Leuk. Lymphoma*, vol. 35, no. 5–6, pp. 455–469, Jan. 1999, doi: 10.1080/10428199909169610.

[20] K. Simons and D. Toomre, “Lipid Rafts and Signal Transduction,” *Nat. Rev. Mol. Cell Biol.*, vol. 1, no. 1, pp. 31–41, 2000, doi: http://dx.doi.org.libezproxy2.syr.edu/10.1038/35036052.

[21] S. D. Conner and S. L. Schmid, “Regulated portals of entry into the cell,” *Nature*, vol. 422, no. 6927, pp. 37–44, 2003, doi: 10.1038/nature01451.

[22] T. Tian, A. Harding, K. Inder, S. Plowman, R. G. Parton, and J. F. Hancock, “Plasma membrane nanoswitches generate high-fidelity Ras signal transduction,” *Nat. Cell Biol.*, vol. 9, no. 8, 2007.

[23] A. Kusumi *et al.*, “Dynamic organizing principles of the plasma membrane that regulate signal transduction: Commemorating the fortieth anniversary of singer and nicolson’s

fluid-mosaic model," *Annu. Rev. Cell Dev. Biol.*, vol. 28, pp. 215–250, 2012, doi: 10.1146/annurev-cellbio-100809-151736.

[24] T. Harayama and H. Riezman, "Understanding the diversity of membrane lipid composition," *Nat. Rev. Mol. Cell Biol.*, vol. 19, no. 5, pp. 281–296, 2018, doi: 10.1038/nrm.2017.138.

[25] J. H. Lorent *et al.*, "Plasma membranes are asymmetric in lipid unsaturation, packing and protein shape," *Nat. Chem. Biol.*, vol. 16, no. 6, pp. 644–652, 2020, doi: 10.1038/s41589-020-0529-6.

[26] S. W. Chiu, S. Vasudevan, E. Jakobsson, R. J. Mashl, and H. L. Scott, "Structure of Sphingomyelin Bilayers: A Simulation Study," *Biophys. J.*, vol. 85, no. 6, pp. 3624–3635, 2003, doi: 10.1016/S0006-3495(03)74780-8.

[27] S. A. Pandit, E. Jakobsson, and H. L. Scott, "Simulation of the early of nano-domain formation in mixed bilayers of sphingomyelin, cholesterol, and dioleylphosphatidylcholine," *Biophys. J.*, vol. 87, no. 5, pp. 3312–3322, 2004, doi: 10.1529/biophysj.104.046078.

[28] P. S. Niemelä, M. T. Hyvönen, and I. Vattulainen, "Influence of chain length and unsaturation on sphingomyelin bilayers," *Biophys. J.*, vol. 90, no. 3, pp. 851–863, 2006, doi: 10.1529/biophysj.105.067371.

[29] R. Vácha, M. L. Berkowitz, and P. Jungwirth, "Molecular model of a cell plasma membrane with an asymmetric multicomponent composition: Water permeation and ion effects," *Biophys. J.*, vol. 96, no. 11, pp. 4493–4501, 2009, doi: 10.1016/j.bpj.2009.03.010.

[30] J. D. Perlmutter and J. N. Sachs, "Interleaflet interaction and asymmetry in phase separated lipid bilayers: Molecular dynamics simulations," *J. Am. Chem. Soc.*, vol. 133, no. 17, pp. 6563–6577, 2011, doi: 10.1021/ja106626r.

[31] C. L. Wennberg, D. Van Der Spoel, and J. S. Hub, "Large influence of cholesterol on solute partitioning into lipid membranes," *J. Am. Chem. Soc.*, vol. 134, no. 11, pp. 5351–5361, 2012, doi: 10.1021/ja211929h.

[32] A. Choubey, R. K. Kalia, N. Malmstadt, A. Nakano, and P. Vashishta, "Cholesterol translocation in a phospholipid membrane," *Biophys. J.*, vol. 104, no. 11, pp. 2429–2436, 2013, doi: 10.1016/j.bpj.2013.04.036.

[33] H. I. Ingólfsson *et al.*, "Lipid organization of the plasma membrane," *J. Am. Chem. Soc.*, vol. 136, no. 41, pp. 14554–14559, 2014, doi: 10.1021/ja507832e.

[34] H. Koldsø, D. Shorthouse, J. Hélie, and M. S. P. Sansom, "Lipid Clustering Correlates with Membrane Curvature as Revealed by Molecular Simulations of Complex Lipid Bilayers," *PLoS Comput. Biol.*, vol. 10, no. 10, 2014, doi: 10.1371/journal.pcbi.1003911.

[35] A. J. Sodt, M. L. Sandar, K. Gawrisch, R. W. Pastor, and E. Lyman, "The molecular structure of the liquid-ordered phase of lipid bilayers," *J. Am. Chem. Soc.*, vol. 136, no. 2, pp. 725–732, 2014, doi: 10.1021/ja4105667.

[36] S. Sharma, B. N. Kim, P. J. Stansfeld, M. S. P. Sansom, and M. Lindau, "A coarse grained model for a lipid membrane with physiological composition and leaflet asymmetry," *PLoS One*, vol. 10, no. 12, pp. 1–21, 2015, doi: 10.1371/journal.pone.0144814.

[37] R. Metzler, J. H. Jeon, and A. G. Cherstvy, "Non-Brownian diffusion in lipid membranes: Experiments and simulations," *Biochim. Biophys. Acta - Biomembr.*, vol. 1858, no. 10, pp. 2451–2467, 2016, doi: 10.1016/j.bbamem.2016.01.022.

[38] R. X. Gu, H. I. Ingólfsson, A. H. De Vries, S. J. Marrink, and D. P. Tieleman, "Ganglioside-Lipid and Ganglioside-Protein Interactions Revealed by Coarse-Grained and Atomistic Molecular Dynamics Simulations," *J. Phys. Chem. B*, vol. 121, no. 15, pp. 3262–3275, 2017, doi: 10.1021/acs.jpcb.6b07142.

[39] J. W. Carter, M. A. Gonzalez, N. J. Brooks, J. M. Seddon, and F. Bresme, "Flip-flop asymmetry of cholesterol in model membranes induced by thermal gradients," *Soft Matter*, vol. 16, no. 25, pp. 5925–5932, 2020, doi: 10.1039/d0sm00546k.

[40] S. Seo, M. Murata, and W. Shinoda, "Pivotal Role of Interdigitation in Interleaflet Interactions: Implications from Molecular Dynamics Simulations," *J. Phys. Chem. Lett.*, vol. 11, no. 13, pp. 5171–5176, 2020, doi: 10.1021/acs.jpclett.0c01317.

[41] K. A. Wilson, H. I. MacDermott-Opeskin, E. Riley, Y. Lin, and M. L. O'Mara, "Understanding the Link between Lipid Diversity and the Biophysical Properties of the Neuronal Plasma Membrane," *Biochemistry*, vol. 59, no. 33, pp. 3010–3018, 2020, doi: 10.1021/acs.biochem.0c00524.

[42] A. N. Leonard, E. Wang, V. Monje-Galvan, and J. B. Klauda, "Developing and Testing of Lipid Force Fields with Applications to Modeling Cellular Membranes," *Chem. Rev.*, vol. 119, no. 9, pp. 6227–6269, 2019, doi: 10.1021/acs.chemrev.8b00384.

[43] W. G. Wood, U. Igbavboa, W. E. Müller, and G. P. Eckert, "Cholesterol asymmetry in synaptic plasma membranes," *J. Neurochem.*, vol. 116, no. 5, pp. 684–689, 2011, doi: 10.1111/j.1471-4159.2010.07017.x.

[44] D. Marquardt *et al.*, "Lipid bilayer thickness determines cholesterols location in model membranes," *Soft Matter*, vol. 12, no. 47, pp. 9417–9428, 2016, doi: 10.1039/c6sm01777k.

[45] D. Marquardt, N. Kučerka, S. R. Wassall, T. A. Harroun, and J. Katsaras, “Cholesterol’s location in lipid bilayers,” *Chem. Phys. Lipids*, vol. 199, pp. 17–25, 2016, doi: 10.1016/j.chemphyslip.2016.04.001.

[46] T. L. Steck and Y. Lange, “Transverse distribution of plasma membrane bilayer cholesterol: Picking sides,” *Traffic*, vol. 19, no. 10, pp. 750–760, 2018, doi: 10.1111/tra.12586.

[47] S. Thallmair, H. I. Ingólfsson, and S. J. Marrink, “Cholesterol Flip-Flop Impacts Domain Registration in Plasma Membrane Models,” *J. Phys. Chem. Lett.*, vol. 9, no. 18, pp. 5527–5533, 2018, doi: 10.1021/acs.jpclett.8b01877.

[48] R. X. Gu, S. Baoukina, and D. P. Tieleman, “Cholesterol Flip-Flop in Heterogeneous Membranes,” *J. Chem. Theory Comput.*, vol. 15, no. 3, pp. 2064–2070, 2019, doi: 10.1021/acs.jctc.8b00933.

[49] M. Aghaaminiha, A. M. Farnoud, and S. Sharma, “Quantitative relationship between cholesterol distribution and ordering of lipids in asymmetric lipid bilayers,” *Soft Matter*, vol. 17, no. 10, pp. 2742–2752, 2021, doi: 10.1039/d0sm01709d.

[50] P. S. Niemelä, M. T. Hyvönen, and I. Vattulainen, “Influence of chain length and unsaturation on sphingomyelin bilayers,” *Biophys. J.*, vol. 90, no. 3, pp. 851–863, 2006, doi: 10.1529/biophysj.105.067371.

[51] T. Fujimoto and I. Parmryd, “Interleaflet coupling, pinning, and leaflet asymmetry-major players in plasma membrane nanodomain formation,” *Front. Cell Dev. Biol.*, vol. 4, no. JAN, pp. 1–12, 2017, doi: 10.3389/fcell.2016.00155.

[52] T. Róg *et al.*, “Interdigitation of long-chain sphingomyelin induces coupling of membrane leaflets in a cholesterol dependent manner,” *Biochim. Biophys. Acta - Biomembr.*, vol. 1858, no. 2, pp. 281–288, 2016, doi: 10.1016/j.bbamem.2015.12.003.

[53] S. Chiantia and E. London, “Acyl Chain length and saturation modulate interleaflet coupling in asymmetric bilayers: Effects on dynamics and structural order,” *Biophys. J.*, vol. 103, no. 11, pp. 2311–2319, 2012, doi: 10.1016/j.bpj.2012.10.033.

[54] S. J. Marrink, H. J. Risselada, S. Yefimov, D. P. Tieleman, and A. H. De Vries, “The MARTINI force field: Coarse grained model for biomolecular simulations,” *J. Phys. Chem. B*, vol. 111, no. 27, pp. 7812–7824, 2007, doi: 10.1021/jp071097f.

[55] S. O. Yesylevskyy, L. V. Schäfer, D. Sengupta, and S. J. Marrink, “Polarizable water model for the coarse-grained MARTINI force field,” *PLoS Comput. Biol.*, vol. 6, no. 6, pp. 1–17, 2010, doi: 10.1371/journal.pcbi.1000810.

[56] D. H. De Jong *et al.*, "Improved parameters for the martini coarse-grained protein force field," *J. Chem. Theory Comput.*, vol. 9, no. 1, pp. 687–697, 2013, doi: 10.1021/ct300646g.

[57] S. J. Marrink and D. P. Tieleman, "Perspective on the martini model," *Chem. Soc. Rev.*, vol. 42, no. 16, pp. 6801–6822, 2013, doi: 10.1039/c3cs60093a.

[58] H. Ma, F. J. Irudayanathan, W. Jiang, and S. Nangia, "Simulating Gram-Negative Bacterial Outer Membrane: A Coarse Grain Model," *J. Phys. Chem. B*, vol. 119, no. 46, pp. 14668–14682, 2015, doi: 10.1021/acs.jpcb.5b07122.

[59] K. N. Ibsen, H. Ma, A. Banerjee, E. E. L. Tanner, S. Nangia, and S. Mitragotri, "Mechanism of Antibacterial Activity of Choline-Based Ionic Liquids (CAGE)," *ACS Biomater. Sci. Eng.*, vol. 4, no. 7, pp. 2370–2379, 2018, doi: 10.1021/acsbiomaterials.8b00486.

[60] H. Ma, A. Khan, and S. Nangia, "Dynamics of OmpF Trimer Formation in the Bacterial Outer Membrane of Escherichia coli," *Langmuir*, vol. 34, no. 19, pp. 5623–5634, 2018, doi: 10.1021/acs.langmuir.7b02653.

[61] F. J. Irudayanathan, J. P. Trasatti, P. Karande, and S. Nangia, "Molecular Architecture of the Blood Brain Barrier Tight Junction Proteins-A Synergistic Computational and in Vitro Approach," *J. Phys. Chem. B*, vol. 120, no. 1, pp. 77–88, 2016, doi: 10.1021/acs.jpcb.5b09977.

[62] F. J. Irudayanathan, X. Wang, N. Wang, S. R. Willsey, I. A. Seddon, and S. Nangia, "Self-Assembly Simulations of Classic Claudins - Insights into the Pore Structure, Selectivity, and Higher Order Complexes," *J. Phys. Chem. B*, vol. 122, no. 30, pp. 7463–7474, 2018, doi: 10.1021/acs.jpcb.8b03842.

[63] N. Rajagopal, F. J. Irudayanathan, and S. Nangia, "Computational nanoscopy of tight junctions at the blood–brain barrier interface," *Int. J. Mol. Sci.*, vol. 20, no. 22, 2019, doi: 10.3390/ijms20225583.

[64] N. Rajagopal, F. J. Irudayanathan, and S. Nangia, "Palmitoylation of Claudin-5 Proteins Influences Their Lipid Domain Affinity and Tight Junction Assembly at the Blood-Brain Barrier Interface," *J. Phys. Chem. B*, vol. 123, no. 5, pp. 983–993, 2019, doi: 10.1021/acs.jpcb.8b09535.

[65] N. Rajagopal and S. Nangia, "Obtaining Protein Association Energy Landscape for Integral Membrane Proteins," *J. Chem. Theory Comput.*, vol. 15, no. 11, pp. 6444–6455, 2019, doi: 10.1021/acs.jctc.9b00626.

[66] F. J. Irudayanathan and S. Nangia, "Paracellular Gatekeeping: What Does It Take for an Ion to Pass through a Tight Junction Pore?," *Langmuir*, vol. 36, no. 24, pp. 6757–6764, 2020, doi: 10.1021/acs.langmuir.0c00877.

[67] N. Rajagopal, A. J. Durand, and S. Nangia, “Predicting selectivity of paracellular pores for biomimetic applications,” *Mol. Syst. Des. Eng.*, vol. 5, no. 3, pp. 686–696, 2020, doi: 10.1039/c9me00177h.

[68] C. A. Lopez, A. J. Rzepiela, A. H. De Vries, L. Dijkhuizen, P. H. Hunenberger, and S. J. Marrink, “Martini Coarse-Grained Force Field: Extension to RNA,” *J. Chem. Theory Comput.*, vol. 5, pp. 3195–3210, 2009, doi: 10.1016/j.bpj.2017.05.043.

[69] T. A. Wassenaar, K. Pluhackova, R. Böckmann, S. J. Marrink, and D. P. Tieleman, “Going Backward: An Efficient Multiscale Approach using Reverse Transformation,” *Biophys. J.*, vol. 106, no. 2, p. 640a, 2014, doi: 10.1016/j.bpj.2013.11.3545.

[70] T. A. Wassenaar, H. I. Ingólfsson, R. A. Böckmann, D. P. Tieleman, and S. J. Marrink, “Computational Lipidomics with insane : A Versatile Tool for Generating Custom Membranes for Molecular Simulations,” *J. Chem. Theory Comput.*, vol. 11, pp. 2144–2155, 2015, doi: 10.1021/acs.jctc.5b00209.

[71] M. J. Abraham *et al.*, “Gromacs: High performance molecular simulations through multi-level parallelism from laptops to supercomputers,” *SoftwareX*, vol. 1–2, pp. 19–25, 2015, doi: 10.1016/j.softx.2015.06.001.

[72] G. Bussi, D. Donadio, and M. Parrinello, “Canonical sampling through velocity rescaling,” *J. Chem. Phys.*, vol. 126, no. 1, 2007, doi: 10.1063/1.2408420.

[73] M. Parrinello and A. Rahman, “Polymorphic transitions in single crystals: A new molecular dynamics method,” *J. Appl. Phys.*, vol. 52, no. 12, pp. 7182–7190, 1981, doi: 10.1063/1.328693.

[74] F. Aurenhammer, “Voronoi Diagrams - A Survey of a Fundamental Data Structure,” *ACM Comput. Surv.*, vol. 23, no. 3, pp. 345–405, 1991.

[75] J. C. Fuller, M. Martinez, and R. C. Wade, “On calculation of the electrostatic potential of a phosphatidylinositol phosphate-containing phosphatidylcholine lipid membrane accounting for membrane dynamics,” *PLoS One*, vol. 9, no. 8, 2014, doi: 10.1371/journal.pone.0104778.

[76] R. P. Bradley, D. R. Slochower, P. A. Janmey, and R. Radhakrishnan, “Divalent cations bind to phosphoinositides to induce ion and isomer specific propensities for nano-cluster initiation in bilayer membranes,” *R. Soc. Open Sci.*, vol. 7, no. 5, 2020, doi: 10.1098/rsos.192208.

[77] S. McLaughlin and D. Murray, “Plasma membrane phosphoinositide organization by protein electrostatics,” *Nature*, vol. 438, no. 7068, pp. 605–611, 2005.

[78] F. Sun, C. F. E. Schroer, C. R. Palacios, L. Xu, S. Z. Luo, and S. J. Marrink, “Molecular mechanism for bidirectional regulation of CD44 for lipid raft affiliation by

palmitoylations and PIP2," *PLoS Comput. Biol.*, vol. 16, no. 4, pp. 1–20, 2020, doi: 10.1371/journal.pcbi.1007777.

[79] S. Garg, L. Porcar, A. C. Woodka, P. D. Butler, and U. Perez-Salas, "Noninvasive neutron scattering measurements reveal slower cholesterol transport in model lipid membranes," *Biophys. J.*, vol. 101, no. 2, pp. 370–377, 2011, doi: 10.1016/j.bpj.2011.06.014.

[80] T. L. Steck and Y. Lange, "How slow is the transbilayer diffusion (Flip-Flop) of cholesterol?," *Biophys. J.*, vol. 102, no. 4, pp. 945–946, 2012, doi: 10.1016/j.bpj.2011.10.059.

[81] M. R. Elkins, A. Bandara, G. A. Pantelopulos, J. E. Straub, and M. Hong, "Direct Observation of Cholesterol Dimers and Tetramers in Lipid Bilayers," *J. Phys. Chem. B*, 2021, doi: 10.1021/acs.jpcb.0c10631.

[82] A. V. Samsonov, I. Mihalyov, and F. S. Cohen, "Characterization of cholesterol-sphingomyelin domains and their dynamics in bilayer membranes," *Biophys. J.*, vol. 81, no. 3, pp. 1486–1500, 2001, doi: 10.1016/S0006-3495(01)75803-1.

[83] E. Wang and J. B. Klauda, "Examination of Mixtures Containing Sphingomyelin and Cholesterol by Molecular Dynamics Simulations," *J. Phys. Chem. B*, vol. 121, no. 18, pp. 4833–4844, 2017, doi: 10.1021/acs.jpcb.7b01832.

[84] R. Laxminarayan *et al.*, "Antibiotic resistance — the need for global solutions," *Lancet Infect. Dis. Comm.*, vol. 13, pp. 1057–1098, 2013, doi: 10.1016/S1473-3099(13)70318-9.

[85] J. M. Thomson and R. A. Bonomo, "The threat of antibiotic resistance in Gram-negative pathogenic bacteria: b-lactams in peril!," *Curr. Opin. Microbiol.*, vol. 8, pp. 518–524, 2005, doi: 10.1016/j.mib.2005.08.014.

[86] J. Vergalli *et al.*, "Porins and small- molecule translocation across the outer membrane of Gram-negative bacteria," *Nat. Rev. Microbiol.*, vol. 18, no. 2020, pp. 164–176, 2020, doi: 10.1038/s41579-019-0294-2.

[87] S. Chevalier *et al.*, "Structure , function and regulation of Pseudomonas aeruginosa porins," no. July, pp. 698–722, 2017, doi: 10.1093/femsre/fux020.

[88] Y. Dai *et al.*, "Development of the computational antibiotic screening platform (CLASP) to aid in the discovery of new antibiotics," *Soft Matter*, vol. 17, no. 10, pp. 2725–2736, 2021, doi: 10.1039/d0sm02035d.

[89] E. Krieger and G. Vriend, "New ways to boost molecular dynamics simulations," *J. Comput. Chem.*, vol. 36, no. 13, pp. 996–1007, 2015, doi: 10.1002/jcc.23899.

[90] K. Vanommeslaeghe *et al.*, “CHARMM General Force Field: A Force Field for Drug-Like Molecules Compatible with the CHARMM All-Atom Additive Biological Force Fields,” *J. Comput. Chem. Chem.*, vol. 31, pp. 671–690, 2009, doi: 10.1002/jcc.

[91] H. Ma *et al.*, “Modeling Diversity in Structures of Bacterial Outer Membrane Lipids,” *J. Chem. Theory Comput.*, vol. 13, no. 2, pp. 811–824, 2017, doi: 10.1021/acs.jctc.6b00856.

[92] J. A. Graham, J. W. Essex, and S. Khalid, “PyCGTOOL: Automated Generation of Coarse-Grained Molecular Dynamics Models from Atomistic Trajectories,” *J. Chem. Inf. Model.*, vol. 57, no. 4, pp. 650–656, 2017, doi: 10.1021/acs.jcim.7b00096.

[93] A. H. De Vries, “The MARTINI Force Field: Coarse Grained Model for Biomolecular Simulations,” pp. 7812–7824, 2007, doi: 10.1021/jp071097f.

Vita

Allyson Karmazyn

Education

Syracuse University, College of Engineering and Computer Science

Bioengineering, Master of Science, May 2021

Bioengineering, Bachelor of Science, May 2020

Vanderbilt University, School of Engineering

Doctor of Philosophy, Chemical Engineering, Expected May 2026

Presentations

College of Engineering and Computer Science Research Day, November 2020

SBI Stevenson Poster Session, March 2019

Additional Research Experience

Research Experience for Undergraduates, University of Southern California, Sharada Research Group, Summer 2019

Computational Study on CH Activation with Dicopper Complexes with a research team led by Dr. Shaama Sharada. Ran simulation of enzyme interactions using IQmol and Qchem and analyzed results of multiple inorganic complexes to quantify the chemical mechanism activation energies and compare values against a Histidine Brace simulation.

Honors and Awards

All University Master's Prize, May 2021

Vanderbilt Engineering Graduate Fellowship Recipient, March 2021

SOURCE Grant Recipient, Summer 2020

SOURCE Grant Recipient, November 2020

Syracuse University ECS Dean's List, Spring 2020

Syracuse University ECS Dean's List, Fall 2017

ECS Leadership Scholar Award, 2017

Professional Membership

Order of the Engineer, May 2020 – Present

Society of Women Engineers, December 2017 – Present

Work Experience

Graduate Teaching Assistant – BEN 385, 485, 486, 487, August 2020 – May 2021

TutorMe.com Tutor, April 2020 – Present

Syracuse University CLASS Tutor – General Chemistry II, January 2019 – May 2019

Undergraduate Researcher – Nangia Lab, October 2018 – May 2020

Volunteer Experience

Syracuse University, College of Engineering and Computer Science, Student Excellerator

Phi Sigma Sigma Philanthropy – Phi Sigma Sigma Foundation, March 2018 – May 2020